https://doi.org/10.5194/egusphere-2026-3153
Preprint. Discussion started: 14 August 2026

Assessing the ability of stationary *in situ* ground-based observations to constrain local methane emissions in space and time in New York State

Matthew L. Loman[1], Lee T. Murray[1,2], Peter D. Ivatt[1,3], Róisín Commane[4,5], Andrew Hallward-Driemeier[4], Raghav Dhall[5], Eric M. Leibensperger[6], Nicholas Balasus[7,8], Lucas Estrada[7], Melissa P. Sulprizio[7], Maryann R. Sargent[7], and Felix Vogel[9]

[1]Department of Earth and Environmental Sciences, University of Rochester, Rochester, NY 14627 USA
[2]Department of Physics and Astronomy, University of Rochester, Rochester, NY 14627 USA
[3]Center for Integrated Research Computing, University of Rochester, Rochester, NY 14627 USA
[4]Department of Earth and Environmental Sciences, Columbia University, New York, NY 10027 USA
[5]Lamont-Doherty Earth Observatory, Palisades, NY 10964 USA
[6]Department of Physics and Astronomy, Ithaca College, Ithaca, NY 14850 USA
[7]School of Engineering and Applied Sciences, Harvard University, Cambridge, MA 02138 USA
[8]now at: Carbon Mapper, Pasadena, CA 91105 USA
[9]Climate Research Division, Environment and Climate Change Canada, Toronto, ON M3H 5T4, CAN

Correspondence: Matthew L. Loman (mloman@ur.rochester.edu) and Lee T. Murray (lee.murray@rochester.edu)

Abstract. Reductions in methane (CH_4) emissions are essential to mitigate near-term climate forcing and enable jurisdictions such as New York State (NYS) to meet greenhouse-gas (GHG) reduction targets. This requires quantification of present-day emissions, underpinned by a robust, independent monitoring framework capable of verifying reported reductions. Assessing whether existing observational infrastructure meets these requirements is essential for emissions accounting and policy implementation. Here, we evaluate the ability of stationary *in situ* methane observations, coupled with a Bayesian inverse modeling framework – the Integrated Methane Inversion (IMI) driven by chemistry-transport model GEOS-Chem – to constrain annual methane emissions and trends across NYS for 2018-2024. We develop capacity for the IMI to assimilate hourly measurements from 29 sites, including four new high-precision continuous monitoring stations calibrated according to international standards. Prior methane emissions for NYS are based on the Gridded New York State (GNYS) inventory, which disaggregates the official NYS bottom-up total state methane emissions estimate for 2020. The observational network provides its strongest constraints around the New York City metropolitan area. Aggregated NYS posterior methane emissions are consistent with the GNYS prior within estimated uncertainties; however, we identify localized emission biases, including underestimates in the New York City area ($p < 0.05$) and broad overestimates throughout most of NYS. We detect statistically significant regional trends in select locations, but no robust statewide trend over 2018-2024. These results demonstrate the strengths and limitations of stationary *in situ* monitoring for policy-relevant methane verification and underscore the need for top-down strategies that integrate observations from multiple platforms.

https://doi.org/10.5194/egusphere-2026-3153
Preprint. Discussion started: 14 August 2026

1 Introduction

Greenhouse gas (GHG) emissions must be reduced in order to curb the scope of anthropogenic climate change. Existing GHG reduction policies are insufficient to limit warming to a 1.5°C increase in global mean temperature even with a period of overshoot, and without policy changes it will be challenging to limit mean global warming to 2°C (United Nations Environment Programme, 2024). Methane (CH_4) is the second-most important GHG after carbon dioxide (CO_2) in terms of contribution to anthropogenic climate perturbation (IPCC, 2023). Methane is a short-lived climate forcer with an atmospheric lifetime of about 11 years but, using the Global Warming Potential (GWP) metric, it has 30 ± 11 times the climate impact of CO_2 per unit mass over a period of 100 years, or 82 ± 26 times the climate impact of CO_2 per unit mass over a period of 20 years (IPCC, 2023). Since methane is also a precursor of tropospheric ozone (O_3), which itself is a GHG and surface pollutant, reductions in methane emissions can also improve local air quality (e.g., Fiore et al., 2002; Shindell et al., 2012; Allen et al., 2021; Staniaszek et al., 2022).

Methane has become an attractive target for reducing GHG emissions due to its large climate impact, short atmospheric lifetime, relationship to air quality, and the availability of low-cost emission reduction technologies (e.g., Nisbet et al., 2020). As of January 2026, 160 countries were participants in the Global Methane Pledge, an agreement to take voluntary action to reduce global methane emissions by 30 % from 2020 to 2030 (Global Methane Pledge, 2025). In 2019, New York State (NYS) passed the Climate Leadership and Community Protection Act (CLCPA), which mandates GHG emission reductions in NYS to 60 % of 1990 levels by 2030 under statutory law. In contrast to many other GHG monitoring and reduction plans, the CLCPA requires accounting of total GHG emissions to use the GWP-20, as opposed to the more commonly used GWP-100, amplifying the relative importance of reducing methane emissions in accounting.

The use of satellite retrievals to constrain methane emissions via top-down methods has become increasingly common (e.g., McNorton et al., 2018; Sheng et al., 2018; Albuhaisi et al., 2024; Duren et al., 2025; Hancock et al., 2025; Janardanan et al., 2025). However, successful satellite retrievals are rare in locations with highly variable albedos. In NYS, frequent clouds and seasonal snow, as well as many large lakes and coastlines, present severe challenges for successful satellite retrievals, limiting the data availability for inverse models that use satellite data alone to constrain methane emissions within the state.

In this work, we present the first systematic assessment of the ability of stationary *in situ* methane observations to constrain both methane emissions and emission trends across New York State (NYS). We use the Gridded New York State (GNYS; Loman et al., 2025) methane emissions inventory, alongside long-term stationary *in situ* observations of methane, in order to optimize annual methane emissions in NYS for 2018 through 2024 with the Integrated Methane Inversion (IMI) inverse modeling framework (Varon et al., 2022; Estrada et al., 2025). Our primary objective is to evaluate whether the existing surface observation network alone is sufficient to constrain annual state-scale methane emissions and detect temporal variability relevant to policy verification. The surface network comprises all publicly available stationary *in situ* methane measurements as well as a new dataset of high-precision *in situ* observations from four long-term monitoring sites within NYS that we operate. To enable this analysis, we develop new capabilities within the IMI framework to assimilate stationary *in situ* observations of

https://doi.org/10.5194/egusphere-2026-3153
Preprint. Discussion started: 14 August 2026

methane. We additionally construct a new high-resolution gridded inventory of natural methane emissions from wetlands in eastern North America to serve as a prior estimate for natural sources in the inversion.

Section 2 introduces the datasets used for model input and describes the model framework used. Section 3 presents the results from our modeling and compares them with other work. We conclude with a summary of our findings in Sect. 4.

2 Methods

We use version 2.0 of the Integrated Methane Inversion (IMI) modeling framework (https://carboninversion.com, last accessed June 15, 2026), which is an open-source software tool that performs an analytical Bayesian synthesis inversion using the GEOS-Chem 3-D chemical transport model (CTM; http://geos-chem.org, last accessed June 15, 2026). The IMI was developed to simplify methane emission optimization from satellite observations (Varon et al., 2022; Estrada et al., 2025). First, we develop a new *in situ* observational operator for the IMI using the existing "ObsPack" *in situ* diagnostic (see Sect. 2.5.3), first introduced in GEOS-Chem version 12.2.0 (The International GEOS-Chem User Community, 2019). Second, we combine multiple regional methane inventories, including a new regional wetlands emissions inventory, to use as our prior estimate of methane emissions in the inversion domain shown in Fig. 1a, and optimize emissions for this domain for the years 2018 through 2024 using all available stationary *in situ* observations of methane. Within NYS, we elect to use the GNYS methane emissions inventory of Loman et al. (2025) as the prior for our analysis. The GNYS is a gridded distribution of the emission totals calculated in the NYS Department of Environmental Conservation (DEC)'s Statewide Greenhouse Gas Emissions Reports. This enables a regionally resolved and policy-relevant evaluation of methane emissions that is directly traceable to official state reporting. Furthermore, we are also able to evaluate and inform the methods of both the DEC and GNYS methods with this work. We further test for sensitivity to state vector construction (Fig. 5), boundary conditions (Sect. 2.2), meteorological fields (Sect. 2.3), observational subset by time of day (Sect. 2.4), and the possible loss of field sites (Sect. 3.3).

The following subsections describe the model inputs employed in this analysis, including prior estimates of anthropogenic and natural methane emissions (Sect 2.1), boundary conditions (Sect 2.2), meteorological fields (Sect 2.3), and the network of stationary *in situ* observations, which includes both original measurements developed for this study and additional observational datasets (Sect 2.4). Section 2.5 provides a description of the theoretical formulation and implementation of the IMI modeling framework, as well as the new developments introduced for this work.

2.1 Prior emissions estimate

2.1.1 Anthropogenic

Figure 1b shows the spatial extents of the various regional gridded methane emission inventories used to construct the anthropogenic portion of our prior emissions. The individual inventories are aggregated from masks using version 3.9.2 of the Harmonized EMissions COmponent (HEMCO; Keller et al., 2014; Lin et al., 2021). The regional inventories applied are the gridded version of Canada's National Inventory Report (CNIR) to the United Nations Framework Convention on Climate

https://doi.org/10.5194/egusphere-2026-3153
Preprint. Discussion started: 14 August 2026

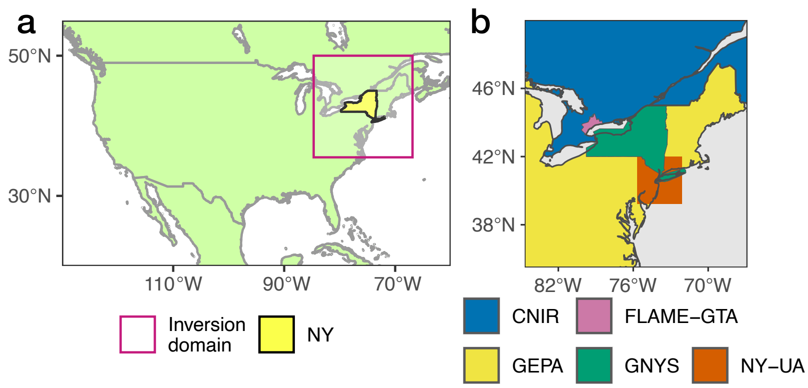

Figure 1. (a) Location of New York State (NYS) and the inversion domain in North America. (b) Locations of regional anthropogenic methane emission inventories used as prior emissions estimates in this work: the gridded version of Canada's National Inventory Report (CNIR), the Facility Level and Area Methane Emissions inventory for the Greater Toronto Area (FLAME-GTA), the gridded version of the US Environmental Protection Agency's Inventory of US Greenhouse Gas Emissions and Sinks (GEPA), the Gridded NYS inventory (GNYS), and the New York City Urban Area inventory (NY-UA). Coastlines and national boundaries are shown in gray in both subplots.

Change for the majority of Canada (Scarpelli et al., 2022b), the Facility Level and Area Methane Emissions inventory for the Greater Toronto Area (FLAME-GTA; Mostafavi Pak et al., 2019, 2021), the Express Extension to the updated gridded version of the US Environmental Protection Agency (EPA)'s Inventory of US Greenhouse Gas Emissions and Sinks (GEPA; Maasakkers et al., 2023), the New York City Urban Area methane emissions inventory (NY-UA; Pitt et al., 2024), and the Gridded New York State methane emissions inventory for within NYS (GNYS; Loman et al., 2025). For any emission categories not present in the regional FLAME-GTA, NY-UA, or GNYS inventories, we default to the CNIR and GEPA inventories for Canada and the US, respectively. We do not use landfill emissions from the FLAME-GTA inventory due to discrepancies with *in situ* observations found by Gillespie et al. (2025). We use the Global Fuel Exploitation Inventory (GFEI; Scarpelli et al., 2022a) for offshore emissions from fossil fuel exploration and production. Offshore emissions from other sources, such as transportation, are included in the CNIR and GEPA inventories for Canada and the US, respectively. We use IMI default prior emissions for anthropogenic emissions from freshwater reservoirs (Delwiche et al., 2022).

2.1.2 Natural

Figure 2 shows the gridded bottom-up wetland methane emission inventory at 0.01° horizontal resolution for northeastern North America developed for this project. In NYS, wetlands are primarily concentrated in lowlands along the northern borders of the state defined by river and lake coastlines. Table 1 summarizes the methane fluxes we assume per wetland type, calculated using the values reported and the wetland type categorization from Tables 13.1, 13A.2, 13A.15, and 15A.2 of the US Global Change Research Program (USGCRP) Second State of the Carbon Cycle Report (SOCCR2; USGCRP, 2018). These fluxes are applied to gridded maps of areal coverage of these five wetland types at 0.01° resolution, which were generated as follows.

https://doi.org/10.5194/egusphere-2026-3153
Preprint. Discussion started: 14 August 2026

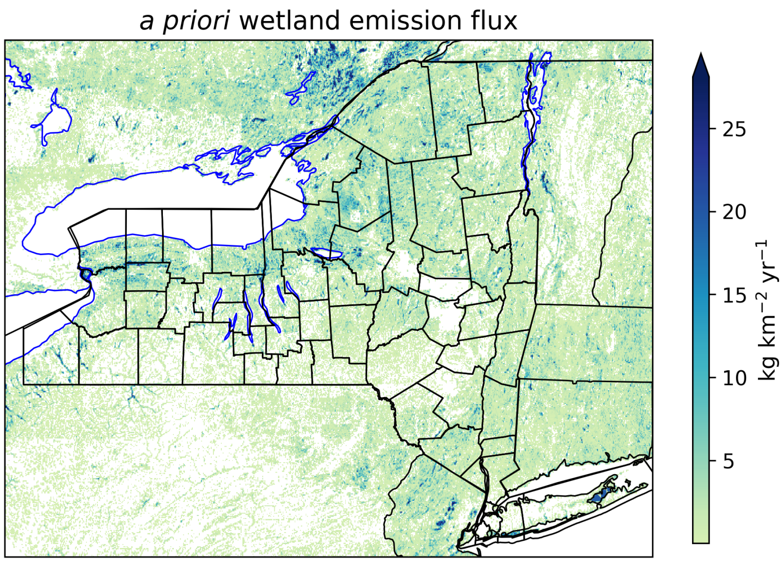

Figure 2. Bottom-up wetland methane emission estimate in kg m^{-2} yr^{-1} used in this study. Methodology is described in the main text. Black lines show state, provincial, and New York county borders. Blue lines show the outlines of large lakes.

Table 1. Mean methane fluxes in kg km^{-2} yr^{-1} by wetland type as categorized in the US Global Change Research Program (USGCRP) Second State of the Carbon Cycle Report (SOCCR2; USGCRP, 2018).

Wetland Type	**CONUS**	**Canada**
Tidal Estuarine	28	28
Emergent Peatland	30	23
Emergent Mineral Soil	35	26
Forested Peatland	12	8.8
Forested Mineral Soil	27	27

For the United States, the US Fish and Wildlife Service (FWS) National Wetlands Inventory (NWI) provides detailed polygon Geographic Information System (GIS) files classifying areal extent of different wetland types for each US state (U.S. Fish and Wildlife Service, 2020). We first spatially merged the files for each state east of the Mississippi River, isolating the polygons for coastal estuary wetlands, emergent wetlands, and forested wetlands. We then used the peatland extent maps from the PEATMAP inventory (Xu et al., 2018) in order to subdivide the emergent wetlands into emergent peatland and emergent mineral soil wetlands, and the forested wetlands into forested peatland and forested mineral soil wetlands. We then rasterized the areal coverage of each wetland type at 0.01° resolution.

For Canada, the Provincial Mapping Unit of the Ontario Ministry of Natural Resources and Forestry provides detailed polygon GIS files classifying areal extents of different wetland types across the entire province (Ontario MNRF, 2020). We

https://doi.org/10.5194/egusphere-2026-3153
Preprint. Discussion started: 14 August 2026

attributed wetlands classified as "fen" or "bog" to emergent peatland, "marsh" to emergent mineral soil, and "unknown" or "swamp" to forested mineral soil. The Québec Ministry of Environment in partnership with Ducks Unlimited Canada provides detailed polygon GIS data for wetlands across southernmost Québec in their "Cartographie des milieux humides du Sud du Québec" product (Ducks Unlimited Canada, 2018). We attributed wetlands classified as "tourbière ouverte bog" or "tourbière ouverte fen" to emergent peatland, "marais" or "prairie humide" to emergent mineral soil, "tourbière boisée" to forested peatland, and "marécage" to forested mineral soil. For boreal Québec and Labrador, we used version 1 of the Boreal-Arctic Wetland and Lake Dataset (BAWLD; Olefeldt et al., 2021a, b), a gridded raster product at 0.5° resolution, and map "bog" and "fen" to emergent peatland and all other wetland classifications to emergent mineral soil. For all remaining locations in Canada, we used the areal extent classifications from Level 3 of the Global Lakes and Wetlands Database (GLWD-3; Lehner and Döll, 2004), a gridded raster product with 30-sec resolution, and map "bog, fen, mire (peatland)" to emergent peatland and "freshwater marsh/floodplain" and "intermittent wetland/lake" to emergent mineral soil. We assumed the remaining partial wetland coverage classifications are distributed evenly between emergent mineral soil and forested mineral soil. We then rasterized the areal coverage of each wetland type at 0.01° resolution, and merge with the United States maps.

Other smaller natural emission sources in the prior include geological seeps from Etiope et al. (2019), scaled to 2 Tg CH_4 yr^{-1} based on Hmiel et al. (2020), open fires from Global Fire Emissions Database version 4 with small fires (GFED4s; Randerson et al., 2017; van der Werf et al., 2017), and termites (Fung, 1991). Since GFED4s was only available through 2023 at the time of this work, we used the Quick Fire Emissions Database version 3.1r1 (QFEDv3.1r1; Darmenov and da Silva, 2015) for open fire emissions in 2024.

2.2 Boundary conditions

In regional modeling, boundary conditions are a necessary input that dictate the state of a given variable at the boundary of the region of interest. In the context of this work, boundary conditions provide mixing ratios of methane immediately outside of the modeled region. Although the IMI optionally includes adjustments to boundary methane mixing ratios in its optimization, high uncertainty in the boundary conditions can inhibit the model's ability to optimize methane emissions (see Sect. 3.1.1). We used two different sets of boundary conditions to evaluate their uncertainty on our results. The CarbonTracker-CH_4 gridded product is a set of 3-D gridded mixing ratios of methane at 2° latitude × 3° longitude horizontal resolution and 3 hr temporal resolution produced by the posterior simulation of a global inversion of methane emissions of the TM5 model assimilating observations of methane mixing ratios and stable carbon isotopologue abundances (http://gml.noaa.gov/ccgg/carbontracker-ch4/, last accessed June 15, 2026; Peters et al., 2007). We use the CarbonTracker-CH_4 gridded product to prescribe boundary conditions from 01 December 2017 through 31 December 2023, the most recent period available at the time of analysis, thereby enabling simulations for 2018–2023 with a one-month model spin-up. The IMI developers maintain an Amazon Web Services (AWS) database containing methane boundary conditions created using GEOS-Chem and bias-corrected using one of two sets of satellite-derived products: methane column retrievals from the TROPOspheric Monitoring Instrument (TROPOMI) aboard the Sentinel-5 Precursor satellite (https://doi.org/10.5270/S5P-3lcdqiv) or the blended data product created by Balasus et al. (2023) using methane columns from TROPOMI and the Greenhouse gases Observing SATellite (GOSAT) (detailed description

https://doi.org/10.5194/egusphere-2026-3153
Preprint. Discussion started: 14 August 2026

of boundary condition files in Estrada et al., 2025). We use the v2025-03-blended TROPOMI+GOSAT-corrected boundary conditions for simulations spanning 2018–2024. As TROPOMI retrievals become available in April 2018, CarbonTracker-CH_4 boundary conditions are used until 31 March 2018, with a transition to the TROPOMI+GOSAT-corrected boundary conditions thereafter in the 2018 simulation.

2.3 Meteorological fields

We test the sensitivity of our results to two different sets of meteorological reanalysis products from the National Aeronautics and Space Administration (NASA) Global Monitoring and Assimilation Office (GMAO) Goddard Earth Observing System (GEOS) meteorological data. For the majority of our simulations, we use a horizontal resolution of 0.25° latitude × 0.3125° longitude (∼25 km×25 km), driven by the GEOS Forward Processing (GEOS-FP) meteorological fields (Rienecker et al., 2008), which are the default meteorological fields in the IMI. However, version 5.25.1p5 of GEOS-FP introduced a substantial change in the treatment of deep convection, affecting the meteorological fields available to GEOS-Chem beginning on 01 June 2020. To assess and constrain the impact of this change on our simulations, we additionally perform simulations using meteorological fields from the Modern-Era Retrospective analysis for Research and Applications, Version 2 (MERRA-2; Gelaro et al., 2017). These fields are generated using a frozen version of the GEOS-5 model, ensuring temporal consistency, but are available only at a coarser horizontal resolution of 0.5° latitude × 0.625° longitude (∼50 km). For our simulations using MERRA-2 meteorological fields, we simulate only with CarbonTracker-CH_4 boundary conditions because we find that they match the observed methane mixing ratios more closely (2018-2023 mean bias 0.9 ppbv in the CarbonTracker-CH_4 boundary conditions versus 6.3 ppbv in TROPOMI+GOSAT-corrected boundary conditions relative to surface observations listed in Table 2).

2.4 Methane observation network

We use stationary *in situ* observations of methane mixing ratios from multiple sources, described below. For most simulations, we assimilate only afternoon observations (12:00-14:59 local time), when the boundary layer is well-developed (e.g., Bakwin et al., 1998; Miles et al., 2017). However, we also perform sensitivity tests, in which we use all available hourly mean observations to estimate the errors in the simulated boundary layer on our results. We also perform sensitivity tests to determine the impact of closure of surface monitoring sites in external networks used in this study. In January 2025, the U.S. federal government canceled the National Institute of Standards and Technology (NIST) Northeast Corridor (NEC) program that operates the NIST/Earth Networks (EN) sites listed in Table 2. Meanwhile, the Harvard, Pennsylvania State University (PSU), and some of the Environment Climate Change Canada (ECCC) operated sites have also ceased operation in recent years. For this sensitivity test, we include only our operated sites and the two presently operational ECCC sites within our inversion domain (WHT, EGB, DWS, ROC, PSP, LDO; see Table 2 for descriptions).

https://doi.org/10.5194/egusphere-2026-3153
Preprint. Discussion started: 14 August 2026

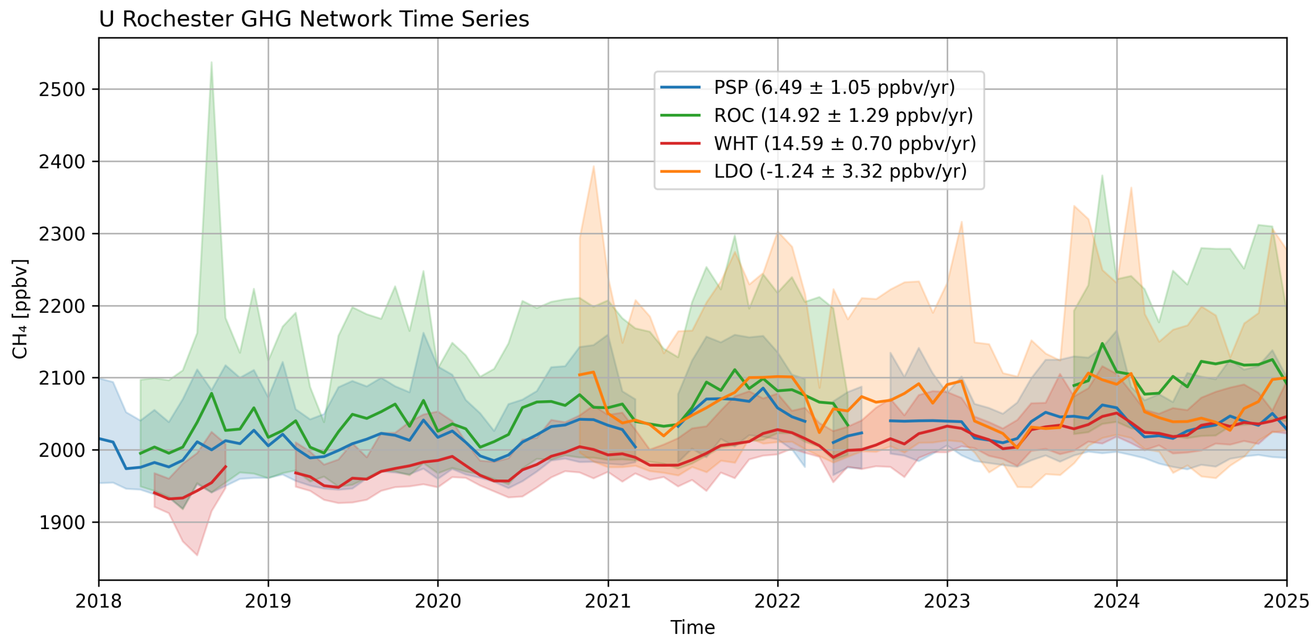

Figure 3. Monthly mean methane mixing ratios (parts per billion by volume; ppbv) measured at four sites in New York State during the study period rise across of most of New York State. Time series are shown as solid lines for our new measurements at Pinnacle State Park (PSP; blue), Rochester (ROC; green), Whiteface Mountain Base (WHT; red), and the Lamont-Doherty Earth Observatory (LDO; orange). Monthly means are calculated from hourly observations for months with at least 360 valid measurements. Shaded ribbons denote the 5^{th}-95^{th} percentile range of hourly methane mixing ratios within each month. Inset values indicate the slope of an ordinary least squares regression of monthly mean mixing ratios versus time (ppbv yr^{-1}), with the uncertainty given as the standard error.

2.4.1 Original measurements

Figure 3 shows the original measurements from our four GHG monitoring sites in New York State, which began in late 2017. The analytical methodology and the physical description of the first three sites are described in detail by Murray and Leibensperger (2020), and were implemented to mimic those of McKain et al. (2015) and Karion et al. (2020). Since that technical report, we established another monitoring site on an emergency communications tower located on the Lamont-Doherty Earth Observatory campus of Columbia University in Palisades, NY, a suburban site to the north-northwest of New York City. In summary, we deployed three Picarro G2301 Cavity Ring Down Spectrometer (CRDS) Analyzers and one Picarro G2110-i CRDS Analyzer to four field sites across New York State. Our locations were chosen to complement the Karion et al. (2020) network (see Sect. 2.4.2), and sited at existing NYS Department of Environmental Conservation (DEC) air quality monitoring stations in order to be co-located with existing National Ambient Air Quality Standards (NAAQS) measurements of other trace gases. We perform an automated 2- or 3-point calibration sequence every 25 hours to standards traceable to the World Meteorological Organization X2004 scale (Dlugokencky et al., 2005). In addition, we manually check all data for

https://doi.org/10.5194/egusphere-2026-3153
Preprint. Discussion started: 14 August 2026

quality assurance, and remove questionable data conservatively by manual inspection. We aggregate data to hourly temporal resolution for analysis.

2.4.2 Additional measurements

In addition to our original continuous measurements, we use all publicly available stationary *in situ* methane data within our domain and time period of analysis (Jan 2018-Jan 2025). The NIST NEC urban test bed project was established in 2015 (Karion et al., 2020). NIST partnered with Earth Networks, Inc. to establish continuous monitoring of methane and carbon dioxide from a network of 32 tall towers with Picarro 2301 CRDS Analyzers extending from North Carolina to New Hampshire, clustered along the Eastern Seaboard. We use here the hourly average product provided by Karion et al. (2025) for the 17 locations closest to New York State. Each tower samples air from at least two inlet heights in an alternating sequence. We also use the hourly methane provided within version 7 of the GLOBALVIEWplus CH_4 ObsPack product aggregated and provided by the US National Oceanic and Atmospheric Administration (NOAA) to the scientific community (Schuldt et al., 2024). The GLOBALVIEWplus methane measurements include calibrated high-precision *in situ* measurements from 67 different laboratories, converted to a consistent ObsPack file format (Masarie et al., 2014). Here we use the GLOBALVIEWplus observations submitted for four sites in Southern Ontario by Environment and Climate Change Canada (ECCC) (Chan et al., 2020; Ishizawa et al., 2024), a tower in northeastern Pennsylvania operated by Penn State University for the Atmospheric Carbon and Transport (ACT)-America campaign (Wei et al., 2021), and three sites in Massachusetts operated by Harvard University (McKain et al., 2015; Sargent et al., 2021).

2.5 Integrated Methane Inversion (IMI)

We use version 2.0 of the Integrated Methane Inversion (IMI) for our inverse modeling (Varon et al., 2022; Estrada et al., 2025). The IMI is open source software for performing analytical methane Bayesian synthesis inversions to optimize methane emissions and, optionally, hydroxyl radical (OH) mixing ratio using version 14.4.1 of chemical transport model GEOS-Chem (Bey et al., 2001; The International GEOS-Chem User Community, 2024) as the forward model and retrievals from the TROPOspheric Monitoring Instrument (TROPOMI https://www.tropomi.eu/) aboard the Sentinel-5 Precursor satellite as the observational input. Version 2.0 of the IMI introduced a variety of improvements and features, including the option to optimize boundary conditions and ability to use the blended TROPOMI+GOSAT data product of Balasus et al. (2023) for boundary conditions (Estrada et al., 2025).

Here, we describe the theoretical basis for an analytical methane Bayesian synthesis inversion (Sect. 2.5.1) and how it is implemented in the IMI for our use case (Sect. 2.5.2). More detail on analytical Bayesian synthesis inversions can be found in Rodgers (2000) and Brasseur and Jacob (2017). More detail on their implementation in the IMI can be found in Varon et al. (2022).

https://doi.org/10.5194/egusphere-2026-3153
Preprint. Discussion started: 14 August 2026

Table 2. Summary of surface monitoring sites we use in this study. Sites are listed from north to south. Site operators are the University of Rochester, Environment and Climate Change Canada (ECCC), the National Institute for Standards and Technology/Earth Networks, Inc. (NIST/EN), Harvard University, and Pennsylvania State University (PSU). Data sources are (a) this study, (b) the CH_4 GLOBALVIEWplus v7.0 ObsPack product (Schuldt et al., 2024), and (c) the NIST Northeast Corridor urban testbed v1.3.0 product (Karion et al., 2020, 2025).

ID	Location	Longitude (°W)	Latitude (°N)	Inlet Height (m.a.g.l.)	Data Availability	Operator	Source
WHT	Whiteface Mtn. Base, Wilmington, NY	73.86	44.39	4	2018-2025	Rochester	a
EGB	Egbert, ON	79.78	44.23	25	2018-2023	ECCC	b
DWS	Downsview, Toronto, ON	79.47	43.78	20	2018-2023	ECCC	b
DNH	Durham, NH	72.15	43.71	121	2018-2025	NIST/EN	c
HNP	Hanlan Point, Toronto, ON	79.39	43.61	10	2018-2021	ECCC	b
ROC	Rochester, NY	77.54	43.15	4	2018-2025	Rochester	a
UNY	Utica, NY	74.79	42.88	64	2018-2025	NIST/EN	c
TPD	Turkey Point, ON	80.56	42.64	35	2018-2021	ECCC	b
HFM	Harvard Forest, Petersham, MA	72.17	42.54	29	2018-2022	Harvard	b
BUN	Boston Univ., Boston, MA	71.10	42.35	29	2018-2022	Harvard	b
COP	Copley Building, Boston, MA	71.08	42.35	260	2018-2022	Harvard	b
PSP	Pinnacle State Park, Addison, NY	77.21	42.09	4	2018-2025	Rochester	a
MSH	Mashpee, MA	70.50	41.66	36	2018-2025	NIST/EN	c
MRC	Mildred, PA	76.42	41.47	61	2018-2022	PSU	b
HCT	Hamden, CT	72.95	41.43	85	2018-2025	NIST/EN	c
SNJ	Stockholm, NJ	74.54	41.14	48	2018-2025	NIST/EN	c
LDO	Lamont-Doherty Earth Obs., Palisades, NY	73.91	41.00	18	2020-2025	Rochester	a
FPL	Flax Pond, Old Field, NY	73.14	40.96	16	2023-2025	NIST/EN	c
LEW	Lewisburg, PA	76.88	40.94	72	2018-2025	NIST/EN	c
MNY	Mineola, NY	73.64	40.75	56	2018-2025	NIST/EN	c
NWK	Newark, NJ	74.17	40.73	143	2023-2025	NIST/EN	c
WNJ	Waterford Works, NJ	74.84	39.73	98	2020-2025	NIST/EN	c
TMD	Thurmont, MD	77.49	39.58	81	2018-2025	NIST/EN	c
NWB	Northwest Baltimore, MD	76.69	39.34	41	2018-2025	NIST/EN	c
NEB	Northeast Baltimore, MD	76.58	39.32	58	2018-2025	NIST/EN	c
HAL	Halethorpe, MD	76.68	39.26	44	2018-2025	NIST/EN	c
JES	Jessup, MD	76.78	39.17	70	2018-2025	NIST/EN	c
BVA	Bluemont, VA	77.83	39.14	50	2021-2025	NIST/EN	c
DER	Derwood, MD	77.14	39.13	44	2018-2025	NIST/EN	c

https://doi.org/10.5194/egusphere-2026-3153
Preprint. Discussion started: 14 August 2026

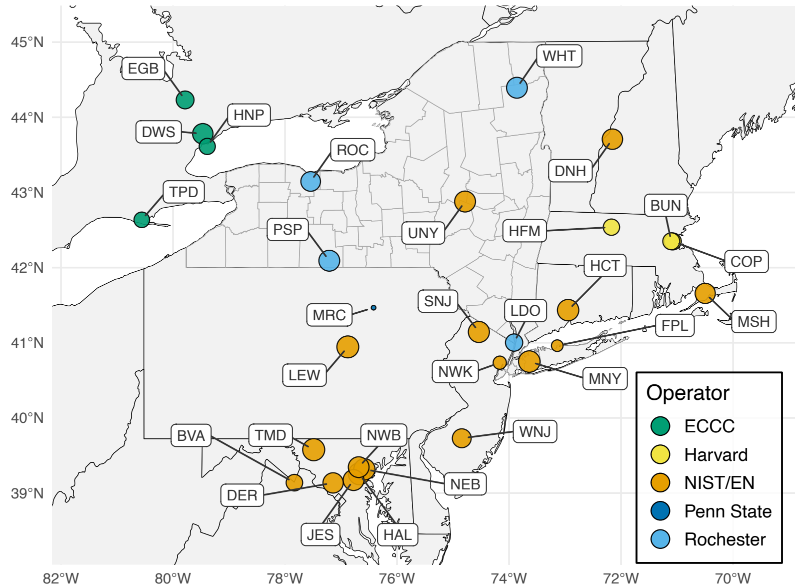

Figure 4. Map of surface *in situ* monitoring sites used in this study. Sites are colored by their operator and their label IDs correspond to Table 2. Black lines show US state and Canadian provincial borders. Light gray lines show New York State county borders. The size of the circle reflects the relative number of observations collected over the Jan 2018 to Jan 2025 period of our analysis.

2.5.1 Analytical inversion

In our model framework, the Bayesian optimal estimate of the state vector $\mathbf{x}$ can be found by minimizing the cost function $J(\mathbf{x})$:

$$J(\mathbf{x}) = (\mathbf{x} - \mathbf{x_a})^{\mathbf{T}} \mathbf{S_a^{-1}} (\mathbf{x} - \mathbf{x_a}) + \gamma [\mathbf{y} - \mathbf{F}(\mathbf{x})]^{\mathbf{T}} \mathbf{S_o^{-1}} [\mathbf{y} - \mathbf{F}(\mathbf{x})]. \tag{1}$$

where $\mathbf{x_a}$ is the prior estimate of the state vector, $\mathbf{S_a}$ is the error covariance matrix of that estimate, γ is a regularization parameter, $\mathbf{y}$ is the observation vector, $\mathbf{F}$ is the forward model that relates the state vector to the observations, and $\mathbf{S_o}$ is the observational error covariance matrix. The regularization parameter γ is included to prevent the overfitting of the solution to observations that can otherwise occur when off-diagonal elements of $\mathbf{S_o}$ and $\mathbf{S_a}$ are not fully characterized.

Analytical inversions of methane, such as those performed with the IMI, assume that the forward model can be approximated as linear since the first-order loss rate of methane is approximately constant due to the relatively narrow range of atmospheric methane mixing ratios. When the forward model is linear, $\mathbf{F}(\mathbf{x})$ in the cost function can be replaced by its derivative, the Jacobian matrix $\mathbf{K} = \nabla_{\mathbf{x}}\mathbf{F} = \frac{\partial \mathbf{y}}{\partial \mathbf{x}}$, because $\mathbf{K}$ is independent of $\mathbf{x}$ in a linear forward model. The optimal estimate $\hat{\mathbf{x}}$ of the state vector, also known as the maximum *a posteriori* (MAP) solution, can then be solved analytically by

$$\hat{\mathbf{x}} = \mathbf{x_a} + \mathbf{G}(\mathbf{y} - \mathbf{K}\mathbf{x_a}), \tag{2}$$

https://doi.org/10.5194/egusphere-2026-3153
Preprint. Discussion started: 14 August 2026

where $\mathbf{G}$ is the gain matrix, which also describes the sensitivity of $\hat{\mathbf{x}}$ to the observations:

$$\mathbf{G} = \left(\mathbf{S_a^{-1}} + \gamma \mathbf{K^T S_o^{-1} K}\right)^{-1} \gamma \mathbf{K^T S_o^{-1}} = \frac{\partial \hat{\mathbf{x}}}{\partial \mathbf{y}}. \tag{3}$$

The product of the gain matrix with the Jacobian matrix $\mathbf{K} = \frac{\partial \mathbf{y}}{\partial \mathbf{x}}$ gives the averaging kernel $\mathbf{A} = \frac{\partial \hat{\mathbf{x}}}{\partial \mathbf{x}}$. The gain matrix and the averaging kernel are useful tools in evaluating inversion results, as they provide the sensitivity of the optimal solution to the observations and to the true value of the state vector, respectively.

This solution to the optimization problem assumes Gaussian errors, which does not exclude negative emissions in the optimal solution (Miller et al., 2014), and methane emissions from oil and gas production have been shown to exhibit lognormal distribution (Yuan et al., 2015). In the IMI, negative posterior emission totals can only be non-physical since soil absorption of methane is not optimized, as there is little information about this sink to be gained from the inversion due to its small magnitude and small spatial gradients (Varon et al., 2022; Estrada et al., 2025). Optimizing $\mathbf{x}' = \ln(\mathbf{x})$ ensures a positive solution and more appropriately represents the heavy-tailed distribution of some methane sources. Since this makes the forward model nonlinear, it is necessary to iterate to find the optimal solution and its error statistics. However, the updated Jacobian matrix $\mathbf{K}'_{(n)} = \frac{\partial \mathbf{y}}{\partial \ln\left(\mathbf{x_{(n)}}\right)}$ for each iteration n has individual elements $\frac{\partial y_i}{\partial \ln(x_j)}$ that are related to the elements of $\mathbf{K}$ by $\frac{\partial y_i}{\partial \ln\left(x_{(n),j}\right)} = x_{(n),j} \frac{\partial y_i}{\partial x_{(n),j}}$, so recalculation of the updated Jacobian matrix for each iteration does not require additional simulations (Maasakkers et al., 2019). Following Rodgers (2000), the solution for each iteration N can be found with the Levenberg-Marquardt method:

$$\mathbf{x}'_{\mathbf{(n+1)}} = \mathbf{x}'_{\mathbf{(n)}} + \left[(\mathbf{1}+\kappa)\mathbf{S_a'^{-1}} + \gamma \mathbf{K'^T_{(n)} S_o^{-1} K'_{(n)}}\right]^{-1} \left[\gamma \mathbf{K'^T_{(n)} S_o^{-1}}\left(\mathbf{y} - \mathbf{K x_{(n)}}\right) - \mathbf{S_a'^{-1}}\left(\mathbf{x}'_{\mathbf{(n)}} - \mathbf{x}'_{\mathbf{a}}\right)\right], \tag{4}$$

where $\mathbf{x}' = \ln(\mathbf{x})$, $\mathbf{x}'_{\mathbf{a}} = \ln(\mathbf{x_a})$, $\mathbf{S}'_{\mathbf{a}} = \ln(\sigma_{\mathbf{a,g}})^2$ with $\sigma_{\mathbf{a,g}}$ as the geometric standard deviation of the prior, and κ is a coefficient for the iterative approach. Solving in lognormal space assumes that $\mathbf{x_a}$ represents the median prior estimate rather than the mean, necessitating a correction to $\mathbf{K}$ using the relationship between the median and mean of a lognormal probability density function:

$$x_{i,\text{median}} = x_{i,\text{mean}} e^{-\frac{\sigma_i^2}{2}}. \tag{5}$$

The IMI uses a constant $\kappa = 10$ following Chen et al. (2022), who found that this constant value leads to faster convergence while yielding the same results as approaches such as those recommended by Rodgers (2000) which gradually decrease κ from some arbitrary starting value. Various methods exist for choosing $\hat{\mathbf{x}}'$ based on the results of the iteration. The IMI adopts the methods of Chen et al. (2022), who set $\hat{\mathbf{x}}' = \mathbf{x}'_{\mathbf{(n+1)}}$ when the maximum difference between elements of $\mathbf{x}'_{\mathbf{(n)}}$ and $\mathbf{x}'_{\mathbf{(n+1)}}$ falls below 0.5 %.

Following Chen et al. (2022) and Rodgers (2000), the posterior error covariance matrix in log space $\hat{\mathbf{S}}'$ can be calculated as:

$$\hat{\mathbf{S}}' = \left(\gamma \mathbf{K'^T S_o^{-1} K'} + \mathbf{S_a'^{-1}}\right)^{-1}. \tag{6}$$

The optimal estimate of a lognormal inversion $\ln(\hat{\mathbf{x}}')$ is the median scale factor, so the IMI applies Eqn. 5 using the diagonal elements of $\hat{\mathbf{S}}'$ to calculate the optimal mean scaling factor estimate.

https://doi.org/10.5194/egusphere-2026-3153
Preprint. Discussion started: 14 August 2026

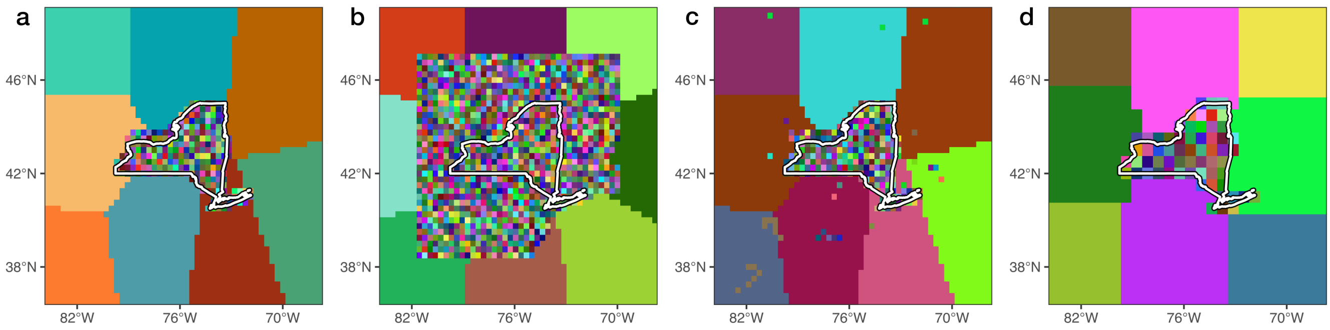

Figure 5. State-vector elements used in this study: (a) 0.25° latitude × 0.3125° longitude, optimizing only NYS at full resolution; (b) 0.25° latitude × 0.3125° longitude, optimizing all non-oceanic cells within 2° of NYS borders at full resolution; (c) 0.25° latitude × 0.3125° longitude, optimizing NYS and all measurement sites at full resolution and clustering large emission sources separately; (d) 0.5° latitude × 0.625° longitude, optimizing only NYS at full resolution. Colors qualitatively indicate different state-vector elements. New York borders shown in white.

2.5.2 Implementation

Figure 5 shows the different state-vector definitions evaluated in this study. The state vector $\mathbf{x}$ is the set of scaling factors applied to all positive methane emissions within these cells, and also includes those for the methane mixing ratios in the boundary conditions at each of the curtain mean values for the four cardinal edges of the inversion domain. The prior estimate of the state vector $\mathbf{x_a}$ is, therefore, a vector of ones of length equal to the number of state-vector elements plus four additional elements to optimize methane mixing ratios coming into the inversion domain across the boundaries. We select as full-resolution (0.25° latitude × 0.3125° longitude; ≈25 km×25 km) state-vector elements all model grid cells that are at least partially within New York State boundaries (including marine and lacustrine cells). When creating the state vector, the IMI groups model grid cells outside the region of interest into "buffer clusters" and assigns a single state-vector element to each cluster. This means that a single scaling factor is optimized for each of these clustered areas and applied to all of the model grid cells it contains. We tested for sensitivity of our results to two alternative definitions of the state vector that allow for greater granularity in the optimized scaling factors in the buffer regions at the computational cost of increasing the number of state-vector elements.

The small state vector (Fig. 5a) is the default treatment in the IMI, in which only model grid cells within the region of interest are optimized at full resolution. The large state vector (Fig. 5b) seeks to optimize a rectangle at full resolution for all non-oceanic grid cells within 2° of the latitude and longitude of NYS borders, an area which also includes all surface measurement locations listed in Table 2 and shown in Fig. 4. The intermediate state vector (Fig. 5c) is an attempt to achieve results similar to the large state vector while reducing the number of elements to a number similar to the small state vector. For these simulations we optimize at full resolution all grid cells inside NYS as well as those containing surface measurement locations outside NYS, and we create additional clusters for model grid cells outside NYS containing emissions of at least 10^{-9} kg CH_4 m^2 s^{-1} (about 20 Gg CH_4 yr^{-1}) from any given source category. This creates three additional clusters

https://doi.org/10.5194/egusphere-2026-3153
Preprint. Discussion started: 14 August 2026

which contain two large landfills to the west of NYS, several reservoirs to the north in Canada, and several coal mines in the Appalachian Mountains to the south, respectively. The MERRA-2 grid state vector is the same as the small state vector, but defined at $0.5°$ latitude $\times$ $0.625°$ longitude resolution ($\approx$50 km$\times$50 km). We use it for our simulations that test the impact of different meteorological fields and horizontal resolution, since it is the native resolution of the MERRA-2 reanalysis.

We apply the forward model (GEOS-Chem version 14.4.1) using prior emissions to generate synthetic observations using an observation operator. We apply our own observation operator to be able to use stationary *in situ* observations in our optimization with the IMI (see Sect. 2.5.3). The difference between the observations and the forward model, $\mathbf{y} - \mathbf{K}\mathbf{x_a}$, is then the innovation or residual term in the MAP solution (Eq. 2).

We select a value for γ based on the work of Lu et al. (2021), who show that the probability density function of the state component $J_\mathbf{a}$ of the cost function can be expected to have a χ^2 distribution with n degrees of freedom, expected value of n, and standard deviation $\sqrt{2n}$, where n is the number of state-vector elements:

$$J_\mathbf{a}(\mathbf{x}) = (\mathbf{x} - \mathbf{x_a})^\mathbf{T} \mathbf{S_a^{-1}} (\mathbf{x} - \mathbf{x_a}) \sim n \pm \sqrt{2n}. \quad (7)$$

Overfitting of the optimal solution to the observations leads to $J_\mathbf{a}(\hat{\mathbf{x}}) \gg n \pm \sqrt{2n}$. We solve for γ iteratively such that $J_\mathbf{a}(\hat{\mathbf{x}})/n \sim 1$ for each individual simulation, as the changes in available observations between years make it impossible to use the same value of γ even when all other variables are held constant.

The IMI computes the Jacobian matrix $\mathbf{K}$ by performing a series of GEOS-Chem simulations in which emission perturbations are applied to grid cells corresponding to one or more elements of the state vector, which are then compared to the base simulation. We apply perturbations to five state-vector elements in each perturbation simulation based on the performance optimization done by the creators of the IMI (Fig. 2 of Estrada et al., 2025). Using our stationary observation operator, the results of these simulations are then sampled at the 3-D coordinates of each measurement to calculate the sensitivity of each site to each state-vector element, $\frac{\Delta y_i}{\Delta x_i}$.

In IMI simulations, the prior $\mathbf{S_a}$ and observational $\mathbf{S_o}$ error covariance matrices are assumed to have no off-diagonal elements and therefore consist of only the error variances of each state-vector element and each site, respectively. This has become common practice in analytical inversions of trace-gas emissions in order to facilitate computation and in the absence of objective information on error covariance (e.g., Souri et al., 2020; Cusworth et al., 2021). The IMI assigns the prior error variance as a single relative value, σ_a^2, assumed constant for all elements of the state vector. We describe our selection of values for prior errors below.

We choose to run the IMI by performing the inversion in a log-transformed space for the state vector in order to guarantee physically appropriate optimal scaling factors for the posterior. Initial attempts in linear space resulted in non-physical negative emissions in select regions. When optimizing a lognormal state vector, the IMI uses geometric standard deviation for state-vector elements, while using arithmetic standard deviation for optimizing boundary conditions and buffer elements, which are treated as additional constraints on boundary conditions and not included in the analysis. Although the IMI only applies the respective 4-D boundary conditions at the edge of the inversion domain, we estimate the error that the boundary conditions may impart on our inversions by sampling them directly at our surface sites within the domain at the time of the observations.

We calculate the root mean square difference of afternoon (12:00-14:59 local time) methane mixing ratios in these virtual samples and the measured values. We use the result, 6 ppbv, as σ_a for the boundary conditions. Since the region of interest for this work matches the extent of the GNYS emissions inventory we use for our prior emissions estimate, we use the equation of Maasakkers et al. (2023) recommended for GNYS by Loman et al. (2025) to find a 95 % relative confidence interval of 53 % for statewide total emissions gridded at $0.25°$ latitude $\times$ $0.3125°$ longitude. For the buffer clusters, which are optimized with normally distributed errors, we use a relative standard deviation of 30 % as a conservative adjustment of this calculation. For all state vector elements within the region of interest, including all the full-resolution elements outside NYS in the large state vector, we translate to a geometric standard deviation σ_g of 1.3 (unitless).

To construct $\mathbf{S_o}$, we calculate the error variance σ_o^2 at each site using the residual method. Total observational error $\boldsymbol{\varepsilon_o}$ is the sum of instrument error, forward model error, and representation error. We assume that all three of these components are randomly distributed about zero and therefore do not contribute to the mean bias of the model $\overline{\mathbf{y}-\mathbf{F}(\mathbf{x})}$, which we assume is due to error in the prior estimate. Therefore, we can obtain total observational error by subtracting mean bias from the difference between observations and prior estimate (e.g., Tarantola, 1987; Palmer et al., 2003; Heald et al., 2004; Brasseur and Jacob, 2017):

$$\boldsymbol{\varepsilon_o} = \mathbf{y} - \mathbf{F}(\mathbf{x_a}) - \overline{\mathbf{y} - \mathbf{F}(\mathbf{x_a})}. \tag{8}$$

We then use σ_o^2, the variance of $\boldsymbol{\varepsilon_o}$ at a given site across the simulation period, to construct $\mathbf{S_o}$. We perform these calculations separately for each simulation.

2.5.3 ObsPack operator

We add an observation operator to the IMI so we can optimize gridded methane emissions using stationary *in situ* methane observations rather than only TROPOMI satellite retrievals. We design this operator to use observations formatted according to the ObsPack framework, which stores observational data from a variety of platforms with internally consistent metadata (Masarie et al., 2014). This allows for compatibility with the existing ObsPack diagnostic output option in GEOS-Chem and reduces output file sizes in the present use case relative to the default IMI satellite observational operator. We edit the IMI code to load and filter daily ObsPack products, enable the ObsPack diagnostic in GEOS-Chem, and use the observational data $\mathbf{y}$ and diagnostic output from the prior run $\mathbf{Kx_a}$ to construct the Jacobian matrix $\mathbf{K}$. We also add the capability to estimate observational error variance on a site-by-site basis in each simulation using the residual method (see Sect. 2.5.2). We use these values to construct the observational error covariance matrix $\mathbf{S_o}$, as opposed to applying a single value to all observations, which is default behavior in the IMI.

3 Results and Discussion

Table 3 summarizes the different combinations of settings we use for our inversions. We conduct sensitivity tests to constrain the impacts of different boundary conditions (Sect. 2.2), meteorological fields (Sect. 2.3), state vectors (Fig. 5), and observational

https://doi.org/10.5194/egusphere-2026-3153
Preprint. Discussion started: 14 August 2026

subsets on our results. We run each annual simulation from Jan 1 of the analysis year to Jan 31 of the subsequent year to ensure that optimized emissions for December are consistent with observational constraints from the following January (except for 2024, in which the simulations end on Dec 31).

3.1 Inversion results

Table 3 shows the mean bias in synthetic observations of methane from simulations using optimized emissions, as well as the interannual mean and standard deviation of degrees of freedom for signal (DOFS) for each multi-year ensemble. Results from the ensemble using TROPOMI+GOSAT boundary conditions and each of the ensembles using only observations from our operated sites and the two operational ECCC sites are excluded for some years due to optimization failure, which we discuss further in Section 3.1.1. The DOFS indicate the number of independent pieces of information provided by the observing system, calculated here for grid cells in NYS and in southeastern NYS where observations are densest (areas $\leq 41.375°$N). We choose this latitude as the cutoff because it is approximately equal to the northernmost extent of the New York City Metropolitan Area. The ensembles that use only afternoon observations tend to have the smallest posterior absolute biases and have DOFS of 4-7 compared to the 249 state-vector elements in NYS. We find that simulations using the small and intermediate state vectors tend to have greater absolute biases despite greater sensitivity to methane emissions within NYS, as indicated by greater mean DOFS, compared to simulations using the large state vector. We also find that mean absolute bias with respect to observations is highest for the simulations that use all observations as opposed to only the afternoon data.

The two ensembles that use the coarser MERRA-2 grid state vector, which differ only in the meteorology used, have the lowest absolute mean biases at NYS sites among all ensembles but larger absolute mean biases across all sites than the other ensembles that use only afternoon observations (Table S1). However, Table S1 also shows higher root mean square error (RMSE) at NYS sites across years for the coarser-resolution ensemble using GEOS-FP meteorology compared to the other ensembles that assimilate only afternoon observations. This indicates that the low absolute mean bias for this ensemble represents more balanced positive and negative biases, rather than better performance. In contrast, the coarser-resolution ensemble using MERRA-2 meteorology has slightly lower RMSE at NYS sites across years relative to the other ensembles using only afternoon observations. Figure S1 shows that this ensemble has RMSE at NYS sites comparable to the other ensembles for 2018-2020 but lower values in 2021-2023 after the change in convection in the GEOS-FP meteorological fields. The lower RMSE of this ensemble is also reflected in its prior simulations, while the change in RMSE from optimization for each year is similar or smaller than other ensembles. These results suggest that the lower absolute mean bias of the coarser-resolution ensemble using MERRA-2 meteorology at NYS sites reflects a decline in performance of the GEOS-FP meteorological fields over NYS concurrent with the change in convection treatment.

The ensembles using CarbonTracker-CH_4 boundary conditions and only afternoon observations allow for a direct evaluation of the impact of state vector choice. The ensemble using the large state vector has both lower absolute mean bias and lower DOFS in NYS compared to the ensembles using the small and medium state vectors. We attribute this difference to the clustered state-vector elements that buffer the region of interest to reduce the bias associated with boundary conditions without large increases in state vector size and computational expense. This method of state vector creation is the default in the IMI and was

https://doi.org/10.5194/egusphere-2026-3153
Preprint. Discussion started: 14 August 2026

Table 3. Summary of ensemble performance and information content for New York State (NYS) inversions. Columns report the mean bias (ppbv) in synthetic methane observations at NYS sites and across all sites, along with the interannual mean (μ) and standard deviation (σ) of the degrees of freedom for signal (DOFS) within NYS and within southeastern NYS ($\leq 41.375°$N). Ensembles that assimilate only afternoon observations exhibit the smallest absolute mean biases and retain the most information content within NYS. Across ensembles, approximately half of the NYS DOFS is concentrated in southeastern NYS, with relatively weak interannual variability in DOFS. Boldface indicates the best-performing ensembles that simulate at 0.25° latitude × 0.3125° longitude resolution, which we use for comparison with other studies (Sect. 3.2).

Meteorology	Boundary conditions	Observation time	Sites	State vector	Time range	Mean bias NYS sites	DOFS $\mu \pm \sigma$ NYS	DOFS $\mu \pm \sigma$ Southeastern NYS[a]
GEOS-FP	**CarbonTracker-CH_4**	**Afternoon**[b]	**All**	**Small**[c]	**2018-2023**	1.6	6.8±1.4	3.4±0.5
GEOS-FP	**CarbonTracker-CH_4**	**Afternoon**	**All**	**Large**[d]	**2018-2023**	-0.1	3.9±0.7	2.0±0.3
GEOS-FP	**CarbonTracker-CH_4**	**Afternoon**	**All**	**Intermediate**[e]	**2018-2023**	0.6	7.0±1.3	3.5±0.4
GEOS-FP	CarbonTracker-CH_4	Afternoon	All	MERRA-2 Grid[f]	2018-2023	-0.1	6.8±1.6	2.8±0.4
MERRA-2	CarbonTracker-CH_4	Afternoon	All	MERRA-2 Grid	2018-2023	0.1	7.2±1.0	2.9±0.4
GEOS-FP	TROPOMI+GOSAT	Afternoon	All	Small	2018-2024[g]	1.0	7.1±1.6	3.7±0.8
GEOS-FP	CarbonTracker-CH_4	All	All	Small	2018-2023	-1.2	8.4±1.2	3.7±0.4
GEOS-FP	CarbonTracker-CH_4	All	All	Large	2018-2023	-2.3	1.6±0.2	0.6±0.1
GEOS-FP	CarbonTracker-CH_4	All	All	Intermediate	2018-2023	-1.5	8.3±1.1	3.7±0.4
GEOS-FP	CarbonTracker-CH_4	Afternoon	UR+ECCC[h]	Small	2018-2023[i]	2.7	5.1±0.4	0.7±1.0
GEOS-FP	CarbonTracker-CH_4	Afternoon	UR+ECCC	Large	2018-2023[j]	-2.1	4.2±0.7	1.0±0.6

[a] $\leq 41.375°$N
[b] 12:00-14:59 Local Time
[c] Figure 5a
[d] Figure 5b
[e] Figure 5c
[f] Figure 5d
[g] Mean bias and DOFS reported for 2020-2024 only
[h] WHT, EGB, DWS, ROC, PSP, LDO; see Table 2
[i] Mean bias and DOFS reported for 2019 and 2021 only
[j] Mean bias and DOFS reported for 2019 and 2021-2023 only

https://doi.org/10.5194/egusphere-2026-3153
Preprint. Discussion started: 14 August 2026

used by Varon et al. (2022) and Estrada et al. (2025) for inversions of the Permian basin and the continental US, respectively. In those studies, clustered buffer elements aggregated grid cells representing regions where emissions and transport errors could reasonably be assumed to be homogeneous, such as rural Texas outside the Permian Basin and the Pacific and Atlantic Oceans. In contrast, the buffer clusters used here encompass heterogeneous regions, combining multiple large urban areas and fossil fuel extraction zones with rural landscapes and extensive bodies of water. Similar to the findings of Nesser et al. (2025), our results indicate that while optimizing large buffer clusters can enhance overall sensitivity, this approach may degrade performance within the region of interest when the assumption of homogeneity is violated.

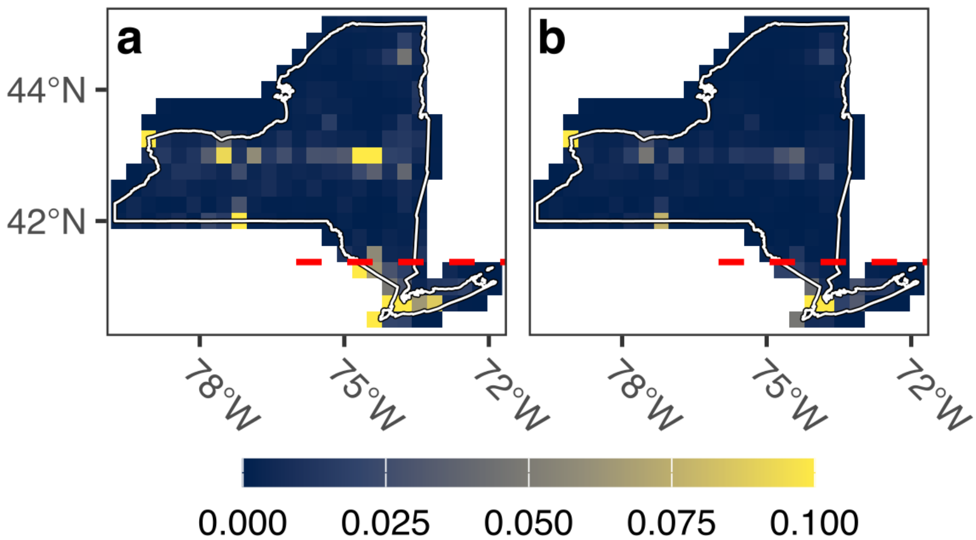

Figure 6. Sensitivity of the optimal state estimate $\hat{\mathbf{x}}$ to the true state, quantified by the diagonal elements of the averaging kernel matrix. Panels show (a) the interannual mean and (b) the interannual standard deviation of the (unitless) averaging kernel diagonals for each state vector grid cell. Sensitivities are largest at measurement locations and in their immediate surroundings, and are small elsewhere, with limited interannual variability. The dashed red line marks the northern boundary used to define southeastern New York State (41.375°N); non-negligible sensitivities south of this latitude indicate that the observing system can best resolve emissions in this region. Results are shown for the ensemble that exhibits the lowest absolute mean bias in simulated observations over New York State (see Table 3).

Figure 6 shows the mean and standard deviation across all years of the diagonal elements of the averaging kernels for the ensemble using GEOS-FP meteorology, CarbonTracker-CH_4 boundary conditions, afternoon observations only, and the large state vector, which exhibits the lowest absolute mean bias. The diagonal elements of the averaging kernel show the sensitivity of the optimal estimate $\hat{\mathbf{x}}$ to the true value of $\mathbf{x}$, or equivalently the ability of the observing system to reduce error relative to the prior estimate $\mathbf{x_a}$. We find that these results are largely consistent over time, with the most notable year-to-year change occurring when Lamont-Doherty Earth Observatory (LDO) observations begin in late 2020, resulting in an increase in DOFS in southeastern NYS close to the measurement location. A group of sites around New York City in the southeast of NYS (Fig. 4)

https://doi.org/10.5194/egusphere-2026-3153
Preprint. Discussion started: 14 August 2026

provides the largest contiguous region of non-negligible sensitivity across all years. The sensitivities of the observing system in all simulations is greatest in the areas immediately surrounding the observation sites themselves, as well as areas with high methane emissions such as Modern Landfill (43.25°N, -79.0625°E) at the western border of NYS and western-central NYS where emissions from landfills, livestock, and wetlands are all relatively high. Although assuming diagonal errors in the prior estimate is in practice a common approximation for the purposes of inverse modeling, the lack of off-diagonal error covariance structure limits the spatial distribution of information that can be gained from a spatially sparse observing system. We can reasonably assume that the observing system is capable of resolving total emissions for areas in which total DOFS is ≥ 1 and sensitivity in the diagonal elements of the averaging kernel is evenly distributed (e.g., Worden et al., 2022). Although this is not the case for NYS as a whole, the area south of 41.375°N in Fig. 6 shows more consistent sensitivity to true emissions, and is responsible for about half of the information content in NYS in the ensembles using observations from all available sites as shown in Table 3. Therefore, we consider that southeastern NYS may be able to meet these criteria. Inclusion of off-diagonal terms in the error covariance matrices in future analyses would likely increase DOFS throughout NYS and may allow this observing system to resolve total emissions for a larger area.

Figure 7 shows the mean prior emissions, the mean posterior emissions, and the mean and interannual standard deviation of the optimized emission scaling factors from the same ensemble as Fig. 6; the results are similar in other ensembles using afternoon observations (Figs. S2, S3, and S4). Methane emissions are overestimated in the prior in most of NYS but underestimated in and around New York City in southeastern NYS. Our optimizations achieve statistically significant ($p < 0.05$) scaling factors only in grid cells adjacent to or containing measurement sites in this ensemble. Higher posterior emissions in New York City are most likely from natural gas end-use emissions that are known to be underestimated in the GNYS inventory (Pitt et al., 2024; Loman et al., 2025). Lower posterior emissions in the rest of the state, where livestock and landfills are the largest methane sources, may reflect the broad spatial distribution of the GNYS inventory of livestock emissions that intentionally ignored information about animal head count in concentrated animal feeding operations (CAFOs) in deference to federal protections for confidential business information. There are hundreds of CAFOs in NYS and their methane emissions can be comparable to combustion facilities (NYSDEC, 2024; Catena et al., 2025). The diffuse treatment of these emissions can lead to overestimates across large areas of NYS, while the lack of underestimates corresponding to CAFO locations may indicate overestimated total livestock emissions, poor sensitivity to these areas from our observations, or both.

Figure 8 shows the time series and 2σ confidence intervals of total prior and posterior emissions for all simulations aggregated over all of NYS (top row) and aggregated over model grid cells in southeastern NYS only (≤ 41.375°N; bottom row). Applying the standard uncertainty propagation that neglects error covariance, as in Sect. 2.5.2, results in a value of 2 % for NYS totals. The method from Maasakkers et al. (2023) that we use to estimate uncertainty in the gridded prior starts with an uncertainty of approximately 23 % for the aggregate total from which the gridded prior was constructed, indicating that error covariance cannot be ignored. Rather than attempt to fully characterize error covariance in both the inversion and aggregated NYS total emissions, we estimate the standard deviation of aggregated emissions as the sum of standard deviations in each model grid cell. This method conservatively assumes that errors across grid cells are 100 % correlated. We use z-statistics to test for statistically significant differences between the prior and posterior emission estimates, and p values from weighted least

https://doi.org/10.5194/egusphere-2026-3153
Preprint. Discussion started: 14 August 2026

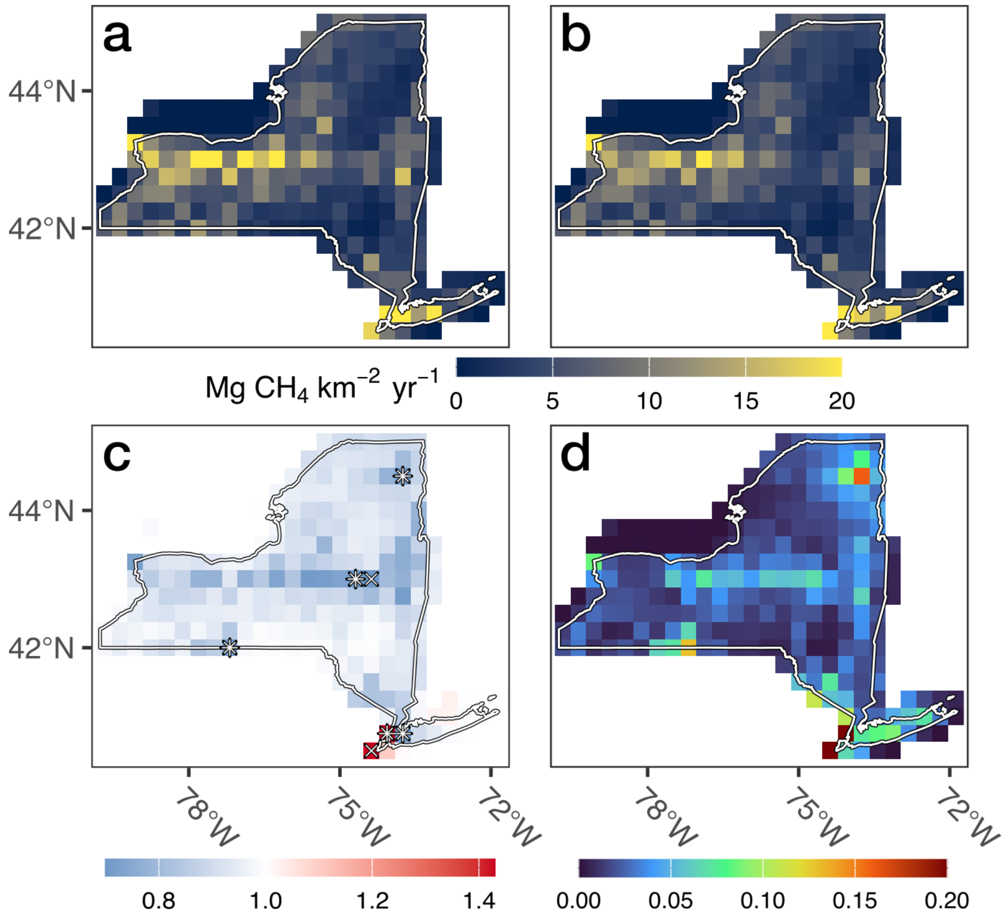

Figure 7. Prior and optimized emissions from the ensemble with the lowest absolute mean bias in simulated observations (see Table 3). (a) Mean total prior emissions across all years; (b) Mean total posterior emissions across all years; scaling factor mean (c) and standard deviation (d) across years of the ensemble. Statistically significant scaling factors in at least one year and at least three years are represented in (c) by grid cells overlaid with × and ∗, respectively.

squares regressions to test for statistically significant trends. We use $p < 0.05$ as the significance threshold for all statistical tests.

Figure 8 shows that the bottom-up inventories we use as prior estimates are consistent with the top-down observations stationary observing system in the whole state for all years, within the uncertainties of the model-observation system. However, we do find statistically significant departures from the prior emissions in our posterior results when focusing on southeastern NYS. The ensembles assimilating only afternoon observations with the small and intermediate state vectors (green lines in the first and third panels on the bottom row) agree that emissions in southeastern NYS were significantly higher than the prior estimate in years 2018-2020 and 2022, while the ensembles using the coarser MERRA-2 grid show significantly higher emissions only in 2021 and 2023, and the ensemble assimilating only afternoon observations with the large state vector shows

https://doi.org/10.5194/egusphere-2026-3153
Preprint. Discussion started: 14 August 2026

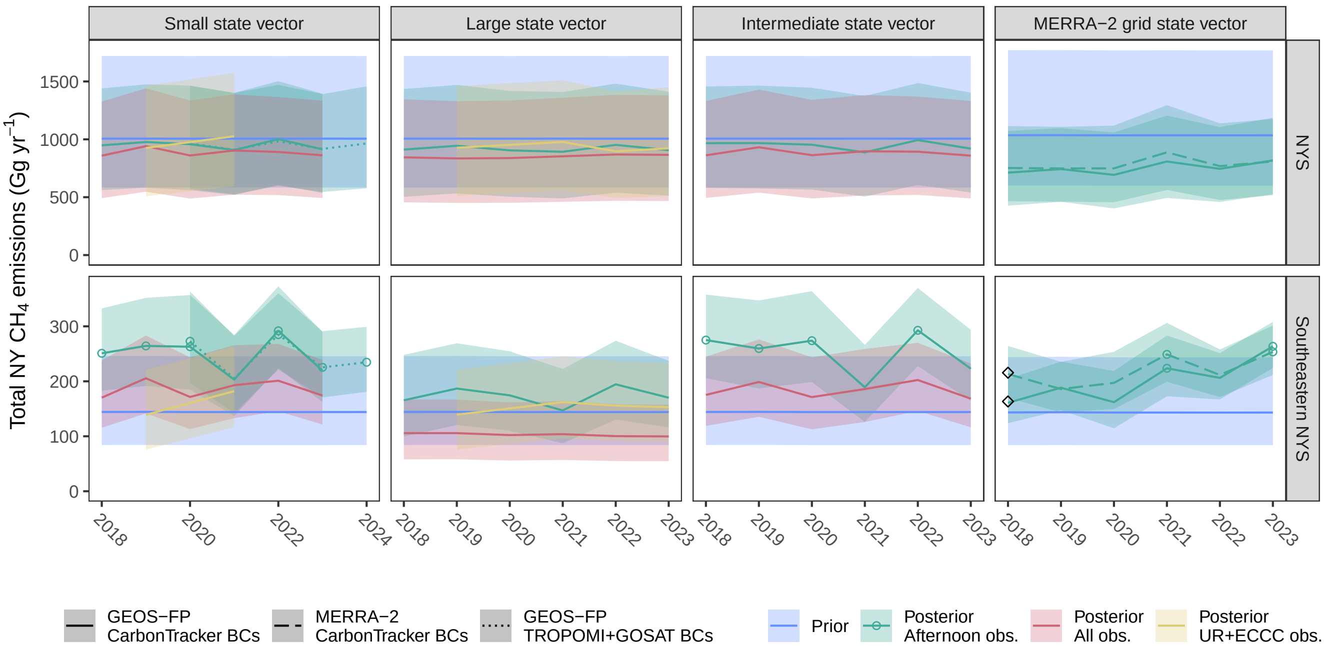

Figure 8. Total prior and posterior methane emissions for all simulations aggregated across NYS (top row) and southeastern NYS ($\leq 41.375°$N; bottom row) indicate statistically significant trends and departures from prior emissions only in southeastern NYS in some simulations. Shaded regions indicate 95 % confidence intervals. Colored circles indicate significantly greater emissions in posterior simulations. Black diamonds indicate posterior simulations with significant differences due to meteorological fields.

no significant departure from the prior estimate at all, indicating that the choice of state vector has a significant impact on inversion results. Significantly different posterior total emissions in southeastern NYS in the coarser-resolution ensembles in 2018 show that the choice of meteorological fields is significant for that year. However, better agreement between these two ensembles in later years and consistency in the years significantly different from the prior indicates that the choice of state vector has a larger impact on posterior total emissions than the choice of meteorological fields and suggests that the update to convection in GEOS-FP may have improved agreement with MERRA-2. Regardless, posterior emissions in southeastern NYS for 2018 from ensembles using GEOS-FP meteorology should be considered less reliable. The ensembles differing only in boundary conditions (solid and dotted green lines in the leftmost column of Fig. 8) show nearly identical results for the four years in which they overlap, indicating a lack of sensitivity to boundary conditions. A least squares regression weighted by posterior uncertainty in each year returns a statistically significant ($p < 0.05$) trend in posterior emissions in southeastern NYS for the ensemble using the MERRA-2 grid driven by GEOS-FP meteorology only. The dependence of any significant trend on our choices of both state vector and meteorology indicates that this result is not reliable.

https://doi.org/10.5194/egusphere-2026-3153
Preprint. Discussion started: 14 August 2026

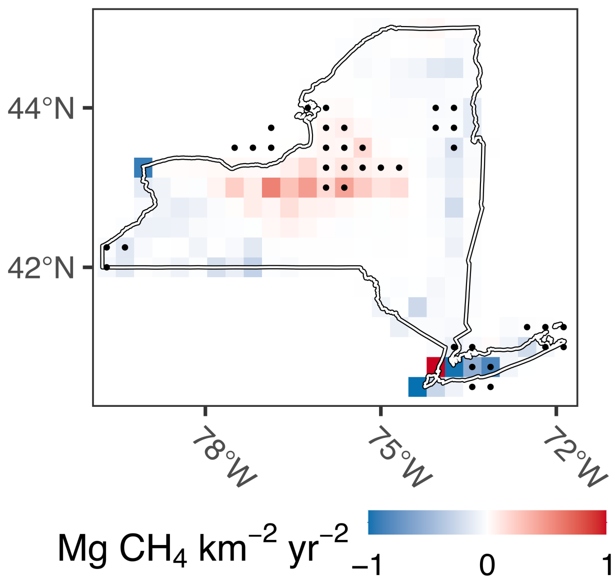

Figure 9. Interannual trends in posterior methane emissions can be seen in areas of southwestern, northeastern, and central NYS, as well as Long Island in the southeast. Stippling indicates statistically significant trends ($p < 0.05$) in the least squares model weighted by posterior uncertainty. Results shown for the ensemble with the lowest absolute mean bias in simulated observations (see Table 3).

Figure 9 shows the interannual trends in posterior methane emissions in each model grid cell in the ensemble using GEOS-FP meteorology, CarbonTracker-CH_4 boundary conditions, afternoon observations only, and the large state vector, with stippling to indicate the statistically significant trends ($p < 0.05$) in a least squares model weighted by posterior uncertainty. A region in central NYS corresponding approximately to the Black River valley, where the primary methane sources in our prior estimate are livestock and fossil fuels, has a small but statistically significant positive trend in annual methane emissions. We find a decreasing trend in annual methane emissions in western Long Island outside New York City in southeastern NYS, where our prior estimate of emissions is dominated by fossil fuel infrastructure. We also find a much smaller negative trend in methane emissions in northeastern NYS, where methane emissions are low but primarily from livestock in the prior estimate. Another slight negative trend in annual emissions with statistical significance is present in southwestern NYS, where the primary source of emissions in the prior estimate is conventional natural gas extraction. However, this is not seen in the results for the corresponding ensembles that use small and intermediate state vectors (Figs. S5 and S6, respectively), which instead show similar significant trends further north, where prior emissions come almost entirely from livestock. Results are otherwise similar for ensembles using GEOS-FP meteorology, CarbonTracker-CH_4 boundary conditions, and only afternoon observations. We consider the statistically significant trends in posterior methane emissions offshore to be essentially meaningless, as their slopes are negligible (on the order of 10^{-7} Mg CH_4 km^{-2} yr^{-2}), reflecting their orders-of-magnitude lower emission estimates than on-shore emissions.

https://doi.org/10.5194/egusphere-2026-3153
Preprint. Discussion started: 14 August 2026

3.1.1 Optimization failure

Our work reveals important considerations for future inverse modeling studies that rely heavily or exclusively on stationary measurements. We find that some combinations of inputs lead to ill-conditioned Hessians of the cost function, characterized by near-zero eigenvalues of $\mathbf{K}^T\mathbf{S}_o^{-1}\mathbf{K}$, indicating poorly constrained directions in state space rather than a robust minimum. This behavior reflects the limited information content of stationary measurements for resolving spatially distributed emissions. Forward model simulations with $\hat{\mathbf{x}}$ calculated from a failed inversion are also unable to consistently reduce absolute mean bias of the model with respect to observations to a value lower than that found in the prior simulations. We find that our inversions are particularly sensitive to prior uncertainty in the boundary conditions, with higher uncertainty of $\sigma_a = 15$ ppbv in the boundary conditions leading to failed inversions for all simulations. We also find that our ability to minimize $J(\mathbf{x})$ is dependent on the number of observation sites used in the inversion, as the ensembles assimilating only UR and ECCC measurements both fail to optimize for 2018 and 2020, and of these, the ensemble that uses the small state vector fails to optimize for 2022-2023 as well.

Although Fig. 8 shows that our inversion results are insensitive to the choice of boundary conditions (i.e., solid vs. dotted lines), this is only the case when the absolute mean bias of the boundary conditions is small. We estimate the contribution of errors in the 4-D boundary conditions by sampling them directly at our surface sites within the domain at the time of the observations, as in our calculation to estimate their prior error in Sect. 2.5.2. For 2018 and 2019, we found that the boundary conditions from the TROPOMI+GOSAT blended product had a mean afternoon (12:00-14:59 local time) bias across all sites of approximately +30 ppbv, compared to -5.5 ppbv for 2021-2024 and -2.6 ppbv in the CarbonTracker-CH_4 boundary conditions for 2018-2019. This is a result of an operational change in the convection scheme in the GEOS-FP meteorological reanalysis that was implemented in 2020, as discussed in Sect. 2.3. This change strongly impacts the resultant surface methane mixing ratios when applying the TROPOMI+GOSAT boundary conditions before and after the change, as these boundary conditions distribute the total methane column of the TROPOMI+GOSAT blended product vertically following a GEOS-Chem simulation driven by GEOS-FP meteorology (Estrada et al., 2025; Shen et al., 2021). The much greater absolute bias of the 2018 and 2019 TROPOMI+GOSAT boundary conditions led to failed optimizations for those years in the ensemble that uses them (see Sect. 3.1.1), so we do not report those results.

3.2 Comparisons with other work

3.2.1 New York State

Figure 10 shows aggregated methane emissions in this study and other gridded inversions that optimize methane emissions over areas that cover at least southeastern NYS at a horizontal resolution of 1° or finer, all of which optimize emissions for 2019. Values for NYS and southeastern NYS are calculated by applying a proportional area mask at the resolution of each study to select only areas inside NYS borders. The confidence intervals for each study are calculated using the same methods with which the data was originally reported, i.e., bootstrapping for Shen et al. (2022), gridded uncertainties for Worden et al. (2022), 2.5 and 97.5-percentile values of flight results for Pitt et al. (2022) and Pitt et al. (2024), and the ensemble range for Nesser et al. (2024). We estimate oil and gas emissions for this study using the same proportions in each grid cell as the prior.

https://doi.org/10.5194/egusphere-2026-3153
Preprint. Discussion started: 14 August 2026

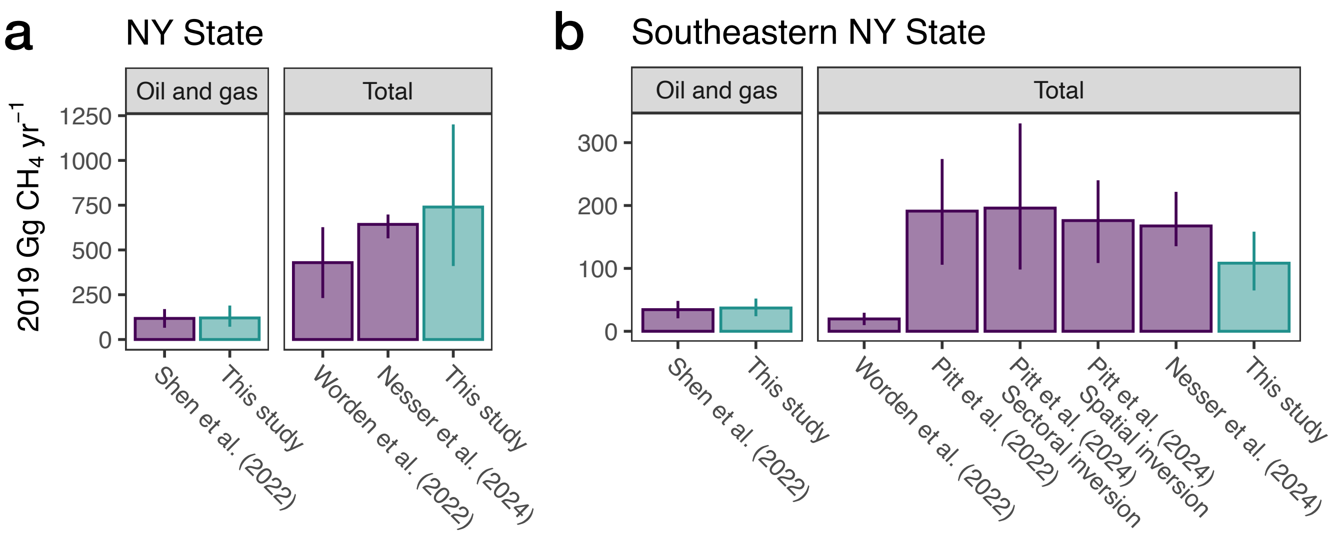

Figure 10. Comparison of 2019 methane emissions aggregated over all of NYS (a) and southeastern NYS (b; $\leq 41.375°$N) in this study and selected gridded inversions. Aggregation is done using a proportional area mask to enable comparison across horizontal resolutions, so values for this study do not match those shown in Fig. 8 which uses a binary mask. Values for this study are calculated as the mean of the three best-performing simulations (see Table 3), with 95 % confidence intervals corresponding to the lowest lower bound and highest upper bound values of the posterior 95 % confidence intervals for 2019 from those ensemble members.

Aggregated emissions in this study are significantly different ($p < 0.05$) from only Worden et al. (2022) in southeastern NYS, which may be an artifact of applying a proportional area mask to coarser resolution (1°) emissions for a small region with high spatial variability. We find here also that using only afternoon observations improves our ability to match other top-down estimates, as repeating this comparison using the ensembles that optimize on all emissions leads to totals for southeastern NYS that are significantly lower than those of Pitt et al. (2022), the spatial inversion of Pitt et al. (2024), and Nesser et al. (2024).

Nesser et al. (2024) also provide the averaging kernels from their TROPOMI inversion ensemble. From their results, we calculate ensemble mean DOFS of 7.6 and 0.8 aggregated over NYS and southeastern NYS, respectively, indicating that the satellite data provides a similar amount of information for the whole state, but less for southeastern NYS relative to this work (see Table 3). This is unsurprising given that southeastern NYS has a large amount of coastline, limiting the success of satellite retrievals in this region. In addition to our findings above that stationary observations alone are insufficient to constrain statewide methane emissions, the comparison with Nesser et al. (2024) indicates that inversions using a single observational platform are not suitable to constrain emissions in NYS. Furthermore, we conclude that this stationary *in situ* observation network fills a vital gap with its capacity to constrain methane emissions in New York City and the surrounding region, where inversions using satellite retrievals have more limited sensitivity.

https://doi.org/10.5194/egusphere-2026-3153
Preprint. Discussion started: 14 August 2026

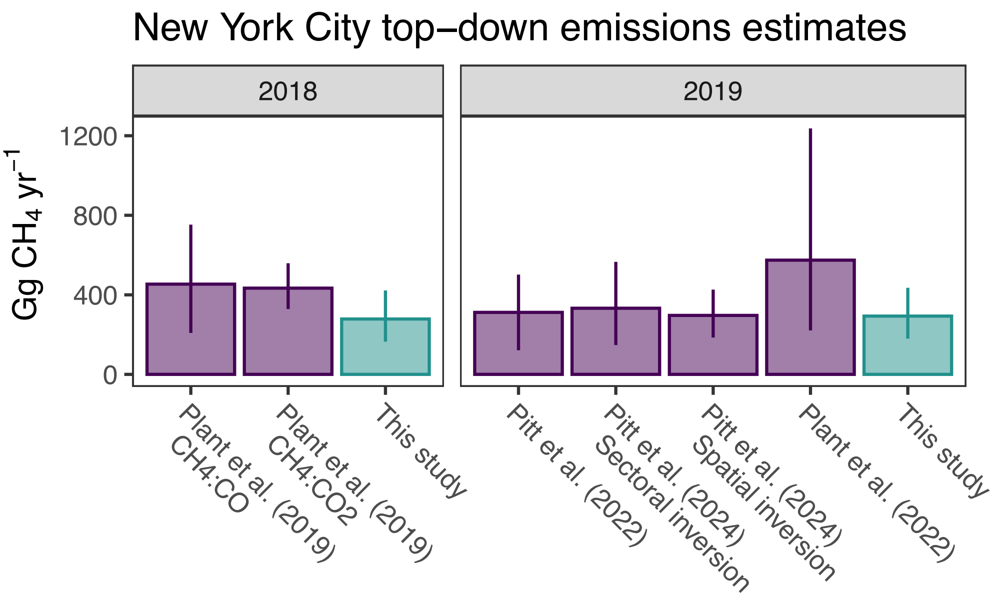

Figure 11. Total estimated emissions (Gg CH_4 yr^{-1}) and 95 % confidence intervals (CI) for the New York City Metropolitan Area in select studies and this study. Studies with observations taken in multiple years are grouped in the year containing the majority of observations. Results from Plant et al. (2019) are labeled with their observed tracer:tracer slope they used to estimate total New York City methane emissions based on inventories of CO and CO_2. Results from Pitt et al. (2024) are labeled with the inversion methods they used, optimizing either total thermogenic (fossil) and non-thermogenic methane emissions (sectoral inversion), and optimizing emissions by grid cell similarly to this work (spatial inversion).

3.2.2 New York City Metropolitan Area

Figure 11 shows the total estimated methane emissions for the New York City Metropolitan Area in this study and other top-down studies (Pitt et al., 2022, 2024; Plant et al., 2019, 2022). In this comparison, values from Pitt et al. (2022, 2024) are aggregated for the New York City Metropolitan Area, while the lower values reported for Pitt et al. (2022, 2024) in Fig. 10b are aggregated for areas within NYS borders and south of 41.375°N. Here we only consider results from our simulations whose configurations have multiple state vector elements in the parts of the New York City Metropolitan Area in adjacent states (i.e., the large state vector), and with afternoon-only observations. We aggregate the posterior emissions from this ensemble as the sum of all grid cells that intersect the New York City Metropolitan Area from the US Census Topologically Integrated Geographic Encoding and Referencing (TIGER) database (U.S. Census Bureau, 2018). Although this may result in an overestimate of the emissions optimized in the New York City Metropolitan Area in this study, we assume that the urban area is responsible for the majority of the emissions from the grid cells that intersect it. Our results show no statistically significant departure ($p > 0.05$) from those of other top-down studies of New York City emissions, although Plant et al. (2019, 2022) estimate higher emissions for the urban area using airborne and satellite tracer-tracer methods. We use the same prior emission estimates as

https://doi.org/10.5194/egusphere-2026-3153
Preprint. Discussion started: 14 August 2026

Pitt et al. (2024) for areas outside NYS and an inventory with similar total emissions for areas inside NYS, indicating that the stationary measurement network is able to provide comparable constraints on metropolitan area emissions as the aircraft observations used by Pitt et al. (2022, 2024). The simulations that assimilate all observations estimate emissions for the New York City Metropolitan Area that are 35 % and 38 % lower than those of that only assimilate afternoon observations for 2018 and 2019, respectively, resulting in totals that are significantly lower than those of Plant et al. (2019, 2022) (Fig. S7). This lends independent support to our finding that the use of all measurements decreases the ability of the inversion to match top-down constraints relative to ensembles that use only afternoon measurements.

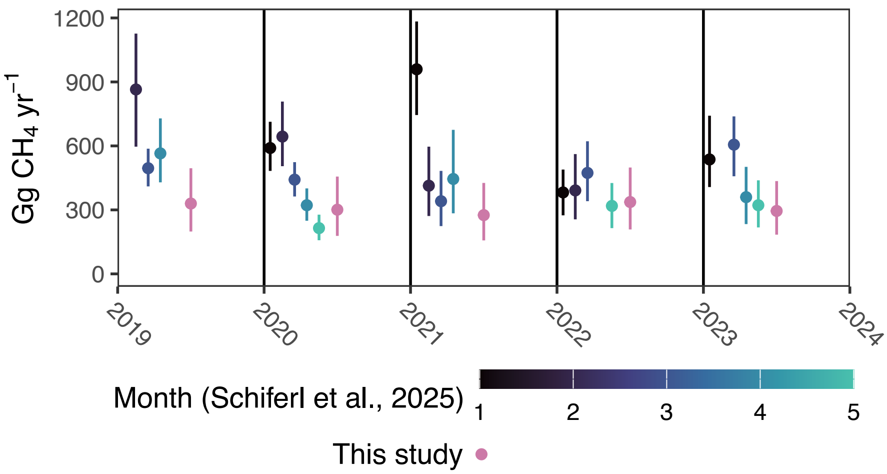

Figure 12. Total estimated emissions (Gg CH_4 yr^{-1}) and 95 % confidence intervals (CI) for the New York City Metropolitan Area (40-42°N, 72.5-75°W) in Schiferl et al. (2025) and this study.

Figure 12 shows total estimated methane emissions for a rectangle (40-42°N, 72.5-75°W) covering the New York City Metropolitan Area in this study and the work of Schiferl et al. (2025). As above, we only consider results from our ensembles whose configurations have multiple state vector elements in the parts of the New York City Metropolitan Area in adjacent states (i.e., large state vector), and with afternoon-only observations. Schiferl et al. (2025) report monthly estimates of methane emissions in this rectangle for 3-5 months between January and May of each year, showing the transition from winter to spring. Our annual mean estimates are generally lower than the respectively monthly estimates in each year. This also provides additional context to the comparison shown in Fig. 11. Plant et al. (2019) used aircraft observations from April-May 2018, while Pitt et al. (2022, 2024) used aircraft observations taken in November, February, and March between November 2018 and March 2020, and Plant et al. (2022) used satellite retrievals taken throughout 2019, with most of these occurring between September and November. Furthermore, the methane emissions estimate of Plant et al. (2022) and one of the Plant et al. (2019) estimates are calculated based on carbon monoxide (CO) emissions estimates from the Emissions Database for Global Atmospheric Research (EDGAR) versions 5.0 and 4.3.2, respectively, using observed methane to CO emission ratios. These estimates are, therefore, also influenced the by seasonal variation in methane to CO emission ratio shown by Schiferl et al.

https://doi.org/10.5194/egusphere-2026-3153
Preprint. Discussion started: 14 August 2026

(2025) as well as the prescribed seasonal cycle in CO emission rates in the EDGAR inventory, and its low bias in total CO emissions in the New York City Metropolitan Area shown by Schiferl et al. (2024). Schiferl et al. (2025) highlight the potential value of utilizing the temporal density of long-term stationary observation networks like the one we use here to constrain methane emissions on shorter-than-annual timescales, as they show seasonal biases in emissions estimates can also suggest specific mitigation measures.

3.2.3 Major point sources

Figure 13 shows a comparison of methane emissions at specific major point sources as previously reported using mass-balance techniques from aerial observations (Catena et al., 2025; Ravikumar et al., 2025) with our mean posterior emissions for the corresponding sector and grid cell. When multiple point sources occupy a single state vector cell, we aggregate the mass-balance estimates before comparison. We roughly estimate prior and posterior emissions for different sectors by applying the same relative proportions of methane emissions for each sector within each grid cell as in the prior inventory. This method assumes the proportions of emissions in each state vector grid cell in the prior inventory are correct. The posterior emissions in this work show limited improvement over the prior estimates for these comparisons, with posterior estimates closer to the 1:1 line in many cases, but for most point sources our posterior estimate is unable to reproduce the emissions estimated via aerial mass balance. This result is expected due to the poor spatial sensitivity of the stationary observing system (Fig. 6), and emissions from compressor stations in particular appear susceptible to biases present in the gridded prior. Estimated emissions from two of the largest landfills in NYS, Modern (43.25°N, -79.0625°E) and Seneca Meadows (43.00°N, -76.8750°E), are annotated in Fig. 13 with (i) and (ii), respectively. Both landfills are associated with relatively high sensitivity in the averaging kernel diagonal, up to 0.28 for Modern and up to 0.22 for Seneca Meadows, indicating that the stationary observations are sensitive to these major point sources despite their distance from the sources. Posterior emissions from Modern are more than 30 % lower than prior emissions, much closer to observed emissions although still significantly higher. However, posterior emissions from Seneca Meadows are virtually unchanged from the prior estimate and remain over 60 % lower than the aerial mass-balance estimate. Catena et al. (2025) report three separate estimates of emissions from each of the two landfills, in June, November, and December of 2021. It appears unlikely that the temporal variability of the landfill emissions not captured by these measurements would lead to this discrepancy in the estimates for Seneca Meadows. However, it is possible that the characterization of agricultural emissions as large area sources in the prior estimate, as mentioned in Section 3.1, may contribute by elevating the modeled background methane and thus decreasing the contribution needed from Seneca Meadows to match the observed mixing ratios. The ability to constrain methane emissions from a wide variety of specific locations is a distinct advantage of spatially dense observations like satellite retrievals.

Although Fig. 7c shows that the inventories we use as our prior emissions overestimate methane emissions in most areas of NYS, our comparison with the aerial mass balance estimates in Fig. 13 indicates that these inventories underestimate several major point sources of methane, mainly landfills. This result suggests diffuse sources of methane as the source of this high bias in our prior emissions. Prior methane emissions from livestock and wetlands, both diffuse sources, have similar totals in NYS, as well as areas of overlap in western NYS where emissions are scaled down the most by our optimization. Uncertainty in

https://doi.org/10.5194/egusphere-2026-3153
Preprint. Discussion started: 14 August 2026

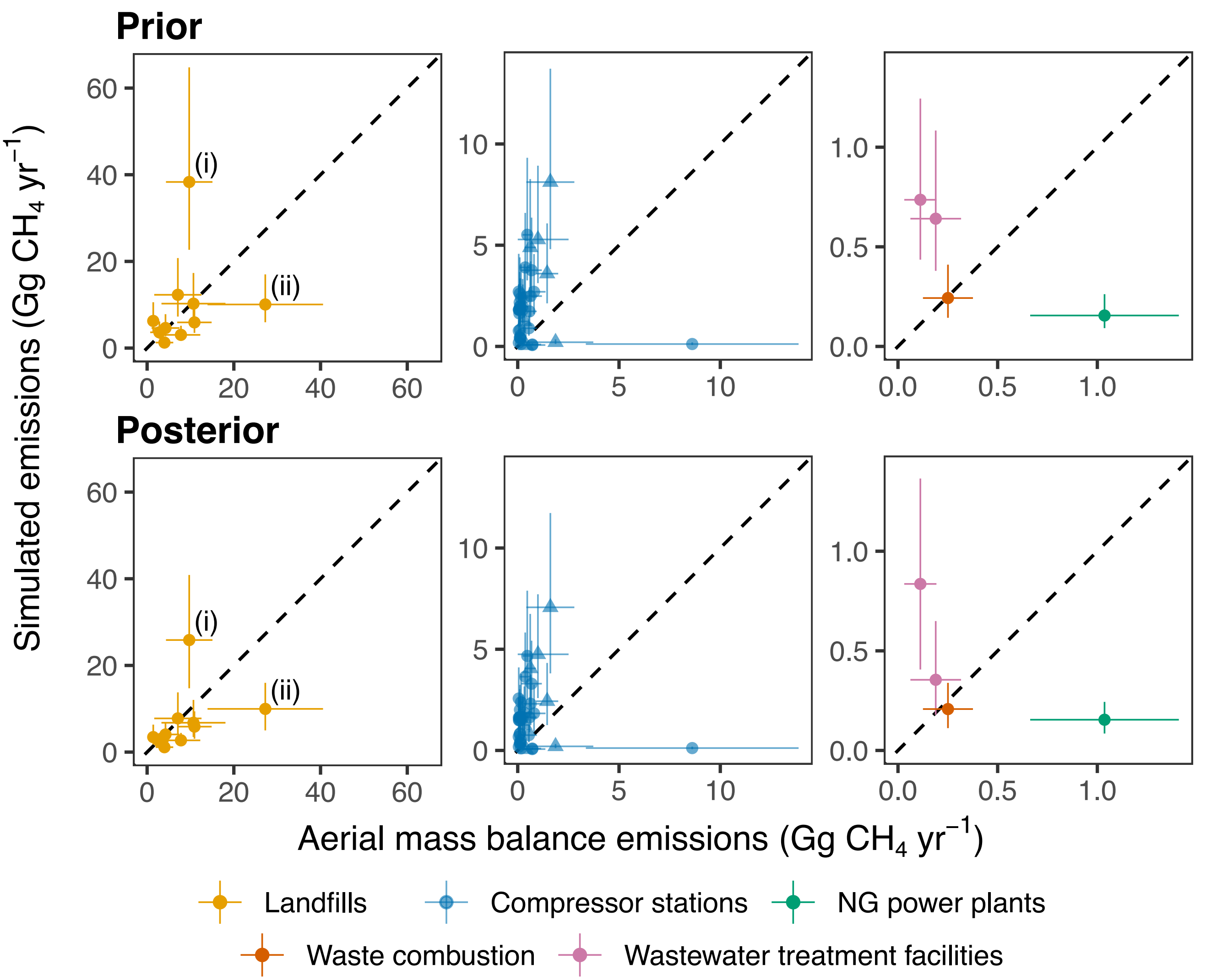

Figure 13. Comparison of methane emissions estimates at specific sites in NYS from this work and aerial mass balance estimates (Catena et al., 2025; Ravikumar et al., 2025). Annotations (i) and (ii) indicate Modern and Seneca Meadows landfills, respectively, the two largest active landfills in NYS by volume. Triangles indicate aggregated emissions for two locations occupying the same simulated grid cell. Values for this study are calculated as the mean of the three best-performing ensembles (see Table 3), with confidence intervals corresponding to the lowest lower bound value and highest upper bound value from those ensemble members. The dashed black line in each plot represents the 1:1 line.

the spatial distribution of livestock emissions in the GNYS inventory likely explains part of this overestimate, but future work optimizing NYS methane emissions using satellite retrievals and finer model resolution is needed to determine which of these methane sources is responsible for the high bias demonstrated by our results.

https://doi.org/10.5194/egusphere-2026-3153
Preprint. Discussion started: 14 August 2026

3.3 What might a future with reduced measurements look like?

Figure 14 shows (a) the interannual mean, (b) standard deviation, and (c) change in interannual mean relative to Fig. 6a of the averaging kernel diagonals for the ensemble limited to only UR and ECCC observations that uses the large state vector, with which we simulate the loss of measurement sites operated by all other organizations, consistent with data availability as of early 2025[1] (see Sect. 2.4). Figure S8 shows the same results for the ensemble using only UR and ECCC observations with the small state vector, with subplot (c) relative to the corresponding ensemble that uses observations from all sites. The most notable differences shown by Fig. 14c are the loss of sensitivity to emissions in eastern NYS and large portions of the New York City Metropolitan Area in the southeast (negative values in blue). However, there is also a broader area of sensitivity (positive values in red) surrounding the Rochester and Pinnacle State Park measurement sites (ROC and PSP in Fig. 4), and corresponding higher mean DOFS statewide in Table 3. This suggests that the Utica measurement site (UNY in Fig. 4) provides conflicting information in the other simulations due to a combination of model transport error and poorly constrained emissions in locations between these sites, thereby reducing the inversion's sensitivity at both locations in ensembles that do use data from the Utica site. Similarly, although sensitivity to emissions in southeastern NYS is lower when fewer observation sites are used, Fig. 14c shows increases in sensitivity to the model grid cell containing the Lamont-Doherty Earth Observatory measurement site and two adjacent cells. Table 3 shows that the ensembles limited to UR and ECCC measurement sites have higher bias with respect to NYS sites compared to the other sites using afternoon observations, despite retaining most of the measurements within NYS. Table 3 also numerically shows the loss of sensitivity in southeastern NYS in these ensembles. Without the NIST/EN sites surrounding New York City, the DOFS indicate that the observing system no longer provides more information on the emissions of southeastern NYS than did TROPOMI in the work of Nesser et al. (2024). This underscores the importance of *in situ* measurement spatial density, including at sites outside NYS, for constraining in-state emissions.

4 Conclusions

We present results from an analytical Bayesian inversion optimizing methane emissions in New York State (NYS) using stationary ground-based measurements of methane mixing ratios from 29 sites in and around the state. We used this framework to assess the extent to which the existing stationary observation network in the recent past can constrain annual methane emissions and emission trends at the state and sub-state scales.

For prior anthropogenic emissions, we aggregated five state-of-the-art regional bottom-up inventories: the Gridded New York State inventory for NYS (GNYS; Loman et al., 2025); the New York Urban Area inventory for metropolitan regions outside NYS (NY-UA; Pitt et al., 2024); the Facility-Level and Area Methane Emissions inventory for the Greater Toronto Area (FLAME-GTA; Mostafavi Pak et al., 2019, 2021); the gridded version of Canada's National Inventory Report for remaining Canadian regions (Scarpelli et al., 2022b); and the Express Extension to the updated gridded US Environmental Protection Agency Inventory of US Greenhouse Gas Emissions and Sinks for the remainder of the United States (GEPA; Maasakkers

[1] NYS has since extended the nine northernmost Earth Networks towers in Table 2 for two more years of sampling following the end of federal support.

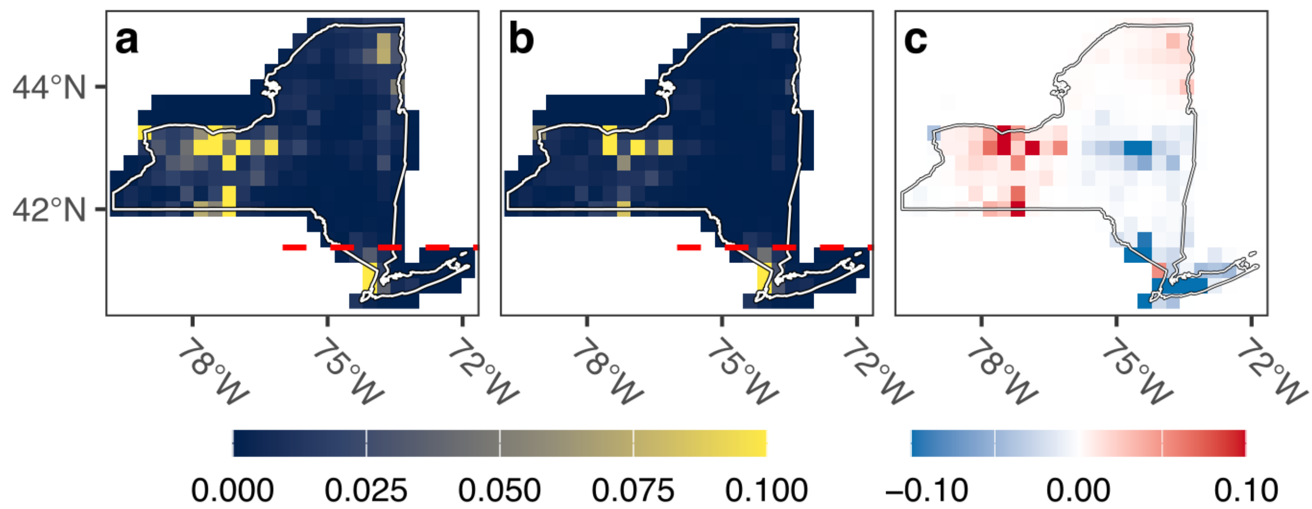

Figure 14. Reduction in information content associated with a reduced observation network, shown by (a) the interannual mean, (b) standard deviation, and (c) change in interannual mean of the averaging-kernel diagonal relative to Fig. 6a for the ensemble using only UR and ECCC observations and the large state vector. Grid cells below the dashed red line are centered south of $41.375°$N. Positive differences indicate locations where the removal of observational constraints reduces the influence of competing information from other sites, rather than reflecting an improvement in observational sensitivity.

et al., 2023). We additionally constructed a new high-resolution gridded inventory of wetland methane emissions for eastern North America to represent natural emissions in the prior.

We introduce a new dataset of original high-precision methane measurements from four long-term *in situ* observation sites in NYS operated by the University of Rochester. The inversion assimilates hourly mean methane mixing ratios from these sites together with all publicly available stationary observations of comparable precision and calibration within the modeling domain that provide coverage between January 2018 and January 2025. We found that the observation network most effectively constrains aggregated methane emissions in southeastern NYS ($\leq 41.375°$N), reflecting the higher density of measurements in this region, with weaker constraints across much of the remainder of the state. Incorporating off-diagonal error covariance terms, particularly in the prior, may improve performance in regions with sparse spatial sampling. We identified statistically significant ($p < 0.05$) interannual emission trends in central NYS, where emissions are increasing, and in western Long Island outside New York City, where emissions are decreasing.

We conducted a series of sensitivity analyses examining the impacts of observation subsets, state vector configuration, boundary conditions, and meteorological fields. Removal of NIST/EN monitoring sites, which constitute the majority of stationary observations used here, together with other recently discontinued sites, severely degraded the ability of stationary observations to constrain aggregated emissions across NYS, particularly in southeastern NYS where our observation network provided the strongest constraints. Sensitivity tests further supported restricting assimilation to afternoon observations, when

https://doi.org/10.5194/egusphere-2026-3153
Preprint. Discussion started: 14 August 2026

the planetary boundary layer is well developed, as evidenced by improved agreement between posterior simulations, consistent with external top-down emission estimates for NYS and the New York City metropolitan area. State vector configuration exerted a strong influence on local and regional posterior emissions and on the total information content of the inversion, indicating that aggregating areas surrounding the region of interest into large clusters for computational efficiency can degrade optimized results within the target region. The choice of meteorological fields had a notable impact on posterior emissions primarily in southeastern NYS in 2018, while sensitivity to boundary conditions depended on the meteorological data used to generate the gridded boundary fields.

Finally, we recommend that future efforts to constrain methane emissions in NYS integrate multiple observational platforms to offset the limitations of individual systems. Stationary observations provide high temporal density that complements the limited retrieval success of spatially dense satellite observations over NYS, while mobile measurements can offer targeted constraints on individual emitters and fill spatial gaps where stationary or satellite observations lack sensitivity. We note that combining heterogeneous observational platforms may require explicit treatment of observational covariance arising from temporal autocorrelation in order to appropriately weight observations with differing averaging timescales.

Code and data availability.

Gridded wetland emissions, methane observations from sites managed by University of Rochester, and inversion results are available at https://doi.org/10.5281/zenodo.20451108.

Author contributions.

MLL: Conceptualization, Methodology, Software, Validation, Formal analysis, Investigation, Data Curation, Writing - Original Draft, Visualization, Project administration

PDI: Methodology, Software, Resources, Formal analysis, Writing - Review & Editing, Supervision, Project administration

LTM: Conceptualization, Methodology, Software, Resources, Data Curation, Writing - Original Draft, Writing - Review & Editing, Supervision, Project administration, Funding acquisition

RC, AHD, RD, EML, MPS, MRS, FV: Data Curation, Writing - Review & Editing

NB, LE: Software, Writing - Review & Editing

Competing interests.

The contact author has declared that none of the authors has any competing interests.

https://doi.org/10.5194/egusphere-2026-3153
Preprint. Discussion started: 14 August 2026

Acknowledgements. We thank Anna Karion and Kimberly Mueller from the National Institute of Standards and Technology (NIST) Special Programs Office for their invaluable contributions to the observation network from the NIST Northeast Corridor Urban Test Bed project. We also thank the University of Rochester Center for Integrated Research Computing (CIRC) for providing computational resources.

Financial support.

This study was funded by the New York State Energy Research and Development Authority (NYSERDA) under contract nos. 100413, 137484, 183865, and 259394.

https://doi.org/10.5194/egusphere-2026-3153
Preprint. Discussion started: 14 August 2026

References

Albuhaisi, Y. A. Y., van der Velde, Y., Pandey, S., and Houweling, S.: Integrating Satellite Observations and Hydrological Models to Unravel Large TROPOMI Methane Emissions in South Sudan Wetlands, Remote Sensing, 16, https://doi.org/10.3390/rs16244744, 2024.

Allen, R. J., Horowitz, L. W., Naik, V., Oshima, N., O'Connor, F. M., Turnock, S., Shim, S., Le Sager, P., van Noije, T., Tsigaridis, K., Bauer, S. E., Sentman, L. T., John, J. G., Broderick, C., Deushi, M., Folberth, G. A., Fujimori, S., and Collins, W. J.: Significant climate benefits from near-term climate forcer mitigation in spite of aerosol reductions, Environmental Research Letters, 16, 034 010, https://doi.org/10.1088/1748-9326/abe06b, 2021.

Bakwin, P. S., Tans, P. P., Hurst, D. F., and Zhao, C.: Measurements of carbon dioxide on very tall towers: results of the NOAA/CMDL program, Tellus B: Chemical and Physical Meteorology, 50, 401–415, https://doi.org/10.3402/tellusb.v50i5.16216, 1998.

Balasus, N., Jacob, D. J., Lorente, A., Maasakkers, J. D., Parker, R. J., Boesch, H., Chen, Z., Kelp, M. M., Nesser, H., and Varon, D. J.: A blended TROPOMI+GOSAT satellite data product for atmospheric methane using machine learning to correct retrieval biases, Atmospheric Measurement Techniques, 16, 3787–3807, https://doi.org/10.5194/amt-16-3787-2023, 2023.

Bey, I., Jacob, D. J., Yantosca, R. M., Logan, J. A., Field, B. D., Fiore, A. M., Li, Q., Liu, H. Y., Mickley, L. J., and Schultz, M. G.: Global modeling of tropospheric chemistry with assimilated meteorology: Model description and evaluation, Journal of Geophysical Research Atmospheres, 106, 23 073–23 095, https://doi.org/10.1029/2001JD000807, 2001.

Brasseur, G. P. and Jacob, D. J.: Modeling of Atmospheric Chemistry, Cambridge University Press, ISBN 978-1-107-14696-9, https://doi.org/10.1017/9781316544754, 2017.

Catena, A. M., Smith, M. L., Murray, L. T., Leibensperger, E. M., Zhang, J., Schwab, M. J., and Schwab, J. J.: Aerial estimates of methane and carbon dioxide emission rates using a mass balance approach in New York State, Earth System Science Data, 17, 4555–4568, https://doi.org/10.5194/essd-17-4555-2025, 2025.

Chan, E., Worthy, D. E. J., Chan, D., Ishizawa, M., Moran, M. D., Delcloo, A., and Vogel, F.: Eight-Year Estimates of Methane Emissions from Oil and Gas Operations in Western Canada Are Nearly Twice Those Reported in Inventories, Environmental Science & Technology, 54, 14 899–14 909, https://doi.org/10.1021/acs.est.0c04117, 2020.

Chen, Z., Jacob, D. J., Nesser, H., Sulprizio, M. P., Lorente, A., Varon, D. J., Lu, X., Shen, L., Qu, Z., Penn, E., and Yu, X.: Methane emissions from China: a high-resolution inversion of TROPOMI satellite observations, Atmospheric Chemistry and Physics, 22, 10 809–10 826, https://doi.org/10.5194/acp-22-10809-2022, 2022.

Cusworth, D. H., Bloom, A. A., Ma, S., Miller, C. E., Bowman, K., Yin, Y., Maasakkers, J. D., Zhang, Y., Scarpelli, T. R., Qu, Z., Jacob, D. J., and Worden, J. R.: A Bayesian framework for deriving sector-based methane emissions from top-down fluxes, Communications Earth & Environment, 2, 242, https://doi.org/10.1038/s43247-021-00312-6, 2021.

Darmenov, A. S. and da Silva, A.: The Quick Fire Emissions Dataset (QFED): Documentation of versions 2.1, 2.2 and 2.4, Tech. Rep. NASA/TM–2015–104606/Vol. 38, Goddard Space Flight Center, National Aeronautics and Space Administration (NASA), data available at https://portal.nccs.nasa.gov/datashare/iesa/aerosol/emissions/QFED/v3.1r1 (accessed 2025-06-11), 2015.

Delwiche, K. B., Harrison, J. A., Maasakkers, J. D., Sulprizio, M. P., Worden, J., Jacob, D. J., and Sunderland, E. M.: Estimating Driver and Pathways for Hydroelectric Reservoir Methane Emissions Using a New Mechanistic Model, Journal of Geophysical Research: Biogeosciences, 127, https://doi.org/10.1029/2022JG006908, 2022.

Dlugokencky, E. J., Myers, R. C., Lang, P. M., Masarie, K. A., Crotwell, A. M., Thoning, K. W., Hall, B. D., Elkins, J. W., and Steele, L. P.: Conversion of NOAA atmospheric dry air CH4 mole fractions to a gravimetrically prepared standard scale, Journal of Geophysical Research: Atmospheres, 110, https://doi.org/10.1029/2005jd006035, 2005.

Ducks Unlimited Canada: Milieux humides cartographie détaillée, [Dataset], https://www.donneesquebec.ca/recherche/dataset/milieux-humides-du-quebec, accessed 05 Oct 2021, 2018.

Duren, R., Cusworth, D., Ayasse, A., Howell, K., Diamond, A., Scarpelli, T., Kim, J., O'neill, K., Lai-Norling, J., Thorpe, A., Zandbergen, S. R., Shaw, L., Keremedjiev, M., Guido, J., Giuliano, P., Goldstein, M., Nallapu, R., Barentsen, G., Thompson, D. R., Roth, K., Jensen, D., Eastwood, M., Reuland, F., Adams, T., Brandt, A., Kort, E. A., Mason, J., and Green, R. O.: The Carbon Mapper emissions monitoring system, Atmospheric Measurement Techniques, 18, 6933–6958, https://doi.org/10.5194/amt-18-6933-2025, 2025.

Estrada, L. A., Varon, D. J., Sulprizio, M., Nesser, H., Chen, Z., Balasus, N., Hancock, S. E., He, M., East, J. D., Mooring, T. A., Alonso, A. O., Maasakkers, J. D., Aben, I., Baray, S., Bowman, K. W., Worden, J. R., Cardoso-Saldaña, F. J., Reidy, E., and Jacob, D. J.: Integrated Methane Inversion (IMI) 2.0: an improved research and stakeholder tool for monitoring total methane emissions with high resolution worldwide using TROPOMI satellite observations, Geoscientific Model Development, 18, 3311–3330, https://doi.org/10.5194/gmd-18-3311-2025, 2025.

Etiope, G., Ciotoli, G., Schwietzke, S., and Schoell, M.: Gridded maps of geological methane emissions and their isotopic signature, Earth System Science Data, 11, https://doi.org/10.5194/essd-11-1-2019, 2019.

Fiore, A. M., Jacob, D. J., Field, B. D., Streets, D. G., Fernandes, S. D., and Jang, C.: Linking ozone pollution and climate change: The case for controlling methane, Geophysical Research Letters, 29, 25–1–25–4, https://doi.org/https://doi.org/10.1029/2002GL015601, 2002.

Fung, I.: Three-dimensional model synthesis of the global methane cycle, Journal of Geophysical Research, 96, https://doi.org/10.1029/91jd01247, 1991.

Gelaro, R., McCarty, W., Suárez, M. J., Todling, R., Molod, A., Takacs, L., Randles, C. A., Darmenov, A., Bosilovich, M. G., Reichle, R., Wargan, K., Coy, L., Cullather, R., Draper, C., Akella, S., Buchard, V., Conaty, A., da Silva, A. M., Gu, W., Kim, G.-K., Koster, R., Lucchesi, R., Merkova, D., Nielsen, J. E., Partyka, G., Pawson, S., Putman, W., Rienecker, M., Schubert, S. D., Sienkiewicz, M., and Zhao, B.: The Modern-Era Retrospective Analysis for Research and Applications, Version 2 (MERRA-2), Journal of Climate, 30, 5419 – 5454, https://doi.org/10.1175/JCLI-D-16-0758.1, 2017.

Gillespie, L. D., Ars, S., Alkadri, S., Urya, S., Khoo, T., Fraser, S., Vogel, F., and Wunch, D.: Estimating methane emissions from the waste sector in Southern Ontario using atmospheric measurements, Journal of the Air & Waste Management Association, 75, 144–163, https://doi.org/10.1080/10962247.2024.2435340, pMID: 39630062, 2025.

Global Methane Pledge: Homepage, https://www.globalmethanepledge.org/, (accessed 2025-06-04), 2025.

Hancock, S. E., Jacob, D. J., Chen, Z., Nesser, H., Davitt, A., Varon, D. J., Sulprizio, M. P., Balasus, N., Estrada, L. A., Cazorla, M., Dawidowski, L., Diez, S., East, J. D., Penn, E., Randles, C. A., Worden, J., Aben, I., Parker, R. J., and Maasakkers, J. D.: Satellite quantification of methane emissions from South American countries: a high-resolution inversion of TROPOMI and GOSAT observations, Atmospheric Chemistry and Physics, 25, 797–817, https://doi.org/10.5194/acp-25-797-2025, 2025.

Heald, C. L., Jacob, D. J., Jones, D. B., Palmer, P. I., Logan, J. A., Streets, D. G., Sachse, G. W., Gille, J. C., Hoffman, R. N., and Nehrkorn, T.: Comparative inverse analysis of satellite (MOPITT) and aircraft (TRACE-P) observations to estimate Asian sources of carbon monoxide, Journal of Geophysical Research D: Atmospheres, 109, 1–17, https://doi.org/10.1029/2004JD005185, 2004.

https://doi.org/10.5194/egusphere-2026-3153
Preprint. Discussion started: 14 August 2026

Hmiel, B., Petrenko, V. V., Dyonisius, M. N., Buizert, C., Smith, A. M., Place, P. F., Harth, C., Beaudette, R., Hua, Q., Yang, B., Vimont, I., Michel, S. E., Severinghaus, J. P., Etheridge, D., Bromley, T., Schmitt, J., Faïn, X., Weiss, R. F., and Dlugokencky, E.: Preindustrial 14CH4 indicates greater anthropogenic fossil CH4 emissions, Nature, 578, 409–412, https://doi.org/10.1038/s41586-020-1991-8, 2020.

https://www.tropomi.eu/: TROPOMI Observing Our Future, (accessed 2025-06-06), 2025.

IPCC: The Earth's Energy Budget, Climate Feedbacks and Climate Sensitivity, p. 923–1054, Cambridge University Press, https://doi.org/10.1017/9781009157896.009, 2023.

Ishizawa, M., Chan, D., Worthy, D., Chan, E., Vogel, F., Melton, J. R., and Arora, V. K.: Estimation of Canada's methane emissions: inverse modelling analysis using the Environment and Climate Change Canada (ECCC) measurement network, Atmospheric Chemistry and Physics, 24, 10 013–10 038, https://doi.org/10.5194/acp-24-10013-2024, 2024.

Janardanan, R., Maksyutov, S., Wang, F., Nayagam, L., Yoshida, Y., Lan, X., and Matsunaga, T.: High-Resolution Inversion of GOSAT-2 Retrievals for Sectoral Methane Emission Estimates During 2019–2022: A Consistency Analysis with GOSAT Inversion, Remote Sensing, 17, https://doi.org/10.3390/rs17172932, 2025.

Karion, A., Callahan, W., Stock, M., Prinzivalli, S., Verhulst, K. R., Kim, J., Salameh, P. K., Lopez-Coto, I., and Whetstone, J.: Greenhouse gas observations from the Northeast Corridor tower network, Earth System Science Data, 12, 699–717, https://doi.org/10.5194/essd-12-699-2020, 2020.

Karion, A., DiGangi, E., Prinzivalli, S., Draper, C., Baldelli, S., Fain, C., Biggs, B., Stock, M., Michalak, B., Salameh, P., Jooil, K., Lueker, T., and Whetstone, J.: Observations of carbon dioxide (CO_2), methane (CH_4), and carbon monoxide (CO) mole fractions from the NIST Northeast Corridor urban testbed, https://doi.org/10.18434/mds2-3765, accessed 15 Apr 2025, 2025.

Keller, C. A., Long, M. S., Yantosca, R. M., Da Silva, A. M., Pawson, S., and Jacob, D. J.: HEMCO v1.0: a versatile, ESMF-compliant component for calculating emissions in atmospheric models, Geoscientific Model Development, 7, 1409–1417, https://doi.org/10.5194/gmd-7-1409-2014, 2014.

Lehner, B. and Döll, P.: Development and validation of a global database of lakes, reservoirs and wetlands, Journal of Hydrology, 296, 1–22, https://doi.org/10.1016/j.jhydrol.2004.03.028, 2004.

Lin, H., Jacob, D. J., Lundgren, E. W., Sulprizio, M. P., Keller, C. A., Fritz, T. M., Eastham, S. D., Emmons, L. K., Campbell, P. C., Baker, B., Saylor, R. D., and Montuoro, R.: Harmonized Emissions Component (HEMCO) 3.0 as a versatile emissions component for atmospheric models: application in the GEOS-Chem, NASA GEOS, WRF-GC, CESM2, NOAA GEFS-Aerosol, and NOAA UFS models, Geoscientific Model Development, 14, 5487–5506, https://doi.org/10.5194/gmd-14-5487-2021, 2021.

Loman, M. L., Murray, L. T., Liebensperger, E. M., and Maasakkers, J. D.: A high-resolution inventory of anthropogenic methane emissions in New York State, Environmental Science & Technology, https://doi.org/10.1021/acs.est.5c07245, 2025.

Lu, X., Jacob, D. J., Zhang, Y., Maasakkers, J. D., Sulprizio, M. P., Shen, L., Qu, Z., Scarpelli, T. R., Nesser, H., Yantosca, R. M., Sheng, J., Andrews, A., Parker, R. J., Boesch, H., Bloom, A. A., and Ma, S.: Global methane budget and trend, 2010-2017: Complementarity of inverse analyses using in situ (GLOBALVIEWplus CH4 ObsPack) and satellite (GOSAT) observations, https://doi.org/10.5194/acp-21-4637-2021, 2021.

Maasakkers, J. D., Jacob, D. J., Sulprizio, M. P., Scarpelli, T. R., Nesser, H., Sheng, J. X., Zhang, Y., Hersher, M., Bloom, A. A., Bowman, K. W., Worden, J. R., Janssens-Maenhout, G., and Parker, R. J.: Global distribution of methane emissions, emission trends, and OH concentrations and trends inferred from an inversion of GOSAT satellite data for 2010-2015, Atmospheric Chemistry and Physics, 19, 7859–7881, https://doi.org/10.5194/acp-19-7859-2019, 2019.

Maasakkers, J. D., McDuffie, E. E., Sulprizio, M. P., Chen, C., Schultz, M., Brunelle, L., Thrush, R., Steller, J., Sherry, C., Jacob, D. J., Jeong, S., Irving, B., and Weitz, M.: A Gridded Inventory of Annual 2012–2018 U.S. Anthropogenic Methane Emissions, Environmental Science & Technology, 57, 16 276–16 288, https://doi.org/10.1021/acs.est.3c05138, 2023.

Masarie, K. A., Peters, W., Jacobson, A. R., and Tans, P. P.: ObsPack: a framework for the preparation, delivery, and attribution of atmospheric greenhouse gas measurements, Earth System Science Data, 6, 375–384, https://doi.org/10.5194/essd-6-375-2014, 2014.

McKain, K., Down, A., Raciti, S. M., Budney, J., Hutyra, L. R., Floerchinger, C., Herndon, S. C., Nehrkorn, T., Zahniser, M. S., Jackson, R. B., Phillips, N., and Wofsy, S. C.: Methane emissions from natural gas infrastructure and use in the urban region of Boston, Massachusetts, Proceedings of the National Academy of Sciences, 112, 1941–1946, https://doi.org/10.1073/pnas.1416261112, 2015.

McNorton, J., Wilson, C., Gloor, M., Parker, R. J., Boesch, H., Feng, W., Hossaini, R., and Chipperfield, M. P.: Attribution of recent increases in atmospheric methane through 3-D inverse modelling, Atmospheric Chemistry and Physics, 18, 18 149–18 168, https://doi.org/10.5194/acp-18-18149-2018, 2018.

Miles, N. L., Richardson, S. J., Lauvaux, T., Davis, K. J., Balashov, N. V., Deng, A., Turnbull, J. C., Sweeney, C., Gurney, K. R., Patarasuk, R., Razlivanov, I., Cambaliza, M. O. L., and Shepson, P. B.: Quantification of urban atmospheric boundary layer greenhouse gas dry mole fraction enhancements in the dormant season: Results from the Indianapolis Flux Experiment (INFLUX), Elementa: Science of the Anthropocene, 5, 27, https://doi.org/10.1525/elementa.127, 2017.

Miller, S. M., Michalak, A. M., and Levi, P. J.: Atmospheric inverse modeling with known physical bounds: an example from trace gas emissions, Geoscientific Model Development, 7, 303–315, https://doi.org/10.5194/gmd-7-303-2014, 2014.

Mostafavi Pak, N., Heerah, S., and Wunch, D.: Methane Emission Inventory for the Greater Toronto Area (GTA), https://doi.org/10.5683/SP2/HTNDSO, 2019.

Mostafavi Pak, N., Heerah, S., Zhang, J., Chan, E., Worthy, D., Vogel, F., and Wunch, D.: The Facility Level and Area Methane Emissions inventory for the Greater Toronto Area (FLAME-GTA), Atmospheric Environment, 252, 118 319, https://doi.org/https://doi.org/10.1016/j.atmosenv.2021.118319, 2021.

Murray, L. T. and Leibensperger, E. M.: Long-Term Monitoring of Methane in New York State: Assessing the Impact of Shifting Energy Portfolios on Regional Air Quality and Climate, Final Report NYSERDA Report 23-21, New York State Energy Research and Development Authority, Albany, NY, https://www.nyserda.ny.gov/About/Newsroom/2020-Reports/2020-04-Long-Term-Monitoring-of-Methane, nYSERDA Contract 100413, 2020.

Nesser, H., Jacob, D. J., Maasakkers, J. D., Lorente, A., Chen, Z., Lu, X., Shen, L., Qu, Z., Sulprizio, M. P., Winter, M., Ma, S., Bloom, A. A., Worden, J. R., Stavins, R. N., and Randles, C. A.: High-resolution US methane emissions inferred from an inversion of 2019 TROPOMI satellite data: contributions from individual states, urban areas, and landfills, Atmospheric Chemistry and Physics, 24, 5069–5091, https://doi.org/10.5194/acp-24-5069-2024, 2024.

Nesser, H., Bowman, K. W., Thill, M. D., Varon, D. J., Randles, C. A., Tewari, A., Cardoso-Saldaña, F. J., Reidy, E., Maasakkers, J. D., and Jacob, D. J.: Predicting and correcting the influence of boundary conditions in regional inverse analyses, Geoscientific Model Development, 18, 9279–9291, https://doi.org/10.5194/gmd-18-9279-2025, 2025.

Nisbet, E. G., Fisher, R. E., Lowry, D., France, J. L., Allen, G., Bakkaloglu, S., Broderick, T. J., Cain, M., Coleman, M., Fernandez, J., Forster, G., Griffiths, P. T., Iverach, C. P., Kelly, B. F. J., Manning, M. R., Nisbet-Jones, P. B. R., Pyle, J. A., Townsend-Small, A., al Shalaan, A., Warwick, N., and Zazzeri, G.: Methane Mitigation: Methods to Reduce Emissions, on the Path to the Paris Agreement, Reviews of Geophysics, 58, e2019RG000 675, https://doi.org/https://doi.org/10.1029/2019RG000675, e2019RG000675 2019RG000675, 2020.

https://doi.org/10.5194/egusphere-2026-3153
Preprint. Discussion started: 14 August 2026

NYSDEC: Concentrated Animal Feeding Operations, https://dec.ny.gov/regulatory/permits-licenses/wastewater-stormwater-water-withdrawal/spdes-permit-program/concentrated-animal-feeding-operations, (accessed 2025-11-13)., 2024.

Olefeldt, D., Hovemyr, M., Kuhn, M., Bastviken, D., Bohn, T., et al.: The fractional land cover estimates from the Boreal-Arctic Wetland and Lake Dataset (BAWLD), 2021, https://doi.org/10.18739/A2C824F9X, accessed 05 Oct 2021, 2021a.

Olefeldt, D., Hovemyr, M., Kuhn, M. A., Bastviken, D., Bohn, T. J., Connolly, J., Crill, P., Euskirchen, E. S., Finkelstein, S. A., Genet, H., Grosse, G., Harris, L. I., Heffernan, L., Helbig, M., Hugelius, G., Hutchins, R., Juutinen, S., Lara, M. J., Malhotra, A., Manies, K., McGuire, A. D., Natali, S. M., O'Donnell, J. A., Parmentier, F.-J. W., Räsänen, A., Schädel, C., Sonnentag, O., Strack, M., Tank, S. E., Treat, C., Varner, R. K., Virtanen, T., Warren, R. K., and Watts, J. D.: The Boreal–Arctic Wetland and Lake Dataset (BAWLD), Earth System Science Data, 13, 5127–5149, https://doi.org/10.5194/essd-13-5127-2021, 2021b.

Ontario MNRF: Wetlands, https://www.ontario.ca/page/open-government-licence-ontario, accessed 02 Oct 2021, 2020.

Palmer, P. I., Jacob, D. J., Jones, D. B. A., Heald, C. L., Yantosca, R. M., Logan, J. A., Sachse, G. W., and Streets, D. G.: Inverting for emissions of carbon monoxide from Asia using aircraft observations over the western Pacific, Journal of Geophysical Research: Atmospheres, 108, https://doi.org/https://doi.org/10.1029/2003JD003397, 2003.

Peters, W., Jacobson, A. R., Sweeney, C., Andrews, A. E., Conway, T. J., Masarie, K., Miller, J. B., Bruhwiler, L. M. P., Pétron, G., Hirsch, A. I., Worthy, D. E. J., van der Werf, G. R., Randerson, J. T., Wennberg, P. O., Krol, M. C., and Tans, P. P.: An atmospheric perspective on North American carbon dioxide exchange: CarbonTracker, Proceedings of the National Academy of Sciences, 104, 18 925–18 930, https://doi.org/10.1073/pnas.0708986104, 2007.

Pitt, J. R., Lopez-Coto, I., Hajny, K. D., Tomlin, J., Kaeser, R., Jayarathne, T., Stirm, B. H., Floerchinger, C. R., Loughner, C. P., Gately, C. K., Hutyra, L. R., Gurney, K. R., Roest, G. S., Liang, J., Gourdji, S., Karion, A., Whetstone, J. R., and Shepson, P. B.: New York City greenhouse gas emissions estimated with inverse modeling of aircraft measurements, Elementa, 10, https://doi.org/10.1525/elementa.2021.00082, 2022.

Pitt, J. R., Lopez-Coto, I., Karion, A., Hajny, K. D., Tomlin, J., Kaeser, R., Jayarathne, T., Stirm, B. H., Floerchinger, C. R., Loughner, C. P., Commane, R., Gately, C. K., Hutyra, L. R., Gurney, K. R., Roest, G. S., Liang, J., Gourdji, S., Mueller, K. L., Whetstone, J. R., and Shepson, P. B.: Underestimation of Thermogenic Methane Emissions in New York City, Environmental Science & Technology, 58, 9147–9157, https://doi.org/10.1021/acs.est.3c10307, 2024.

Plant, G., Kort, E. A., Floerchinger, C., Gvakharia, A., Vimont, I., and Sweeney, C.: Large Fugitive Methane Emissions From Urban Centers Along the U.S. East Coast, Geophysical Research Letters, 46, 8500–8507, https://doi.org/10.1029/2019gl082635, 2019.

Plant, G., Kort, E. A., Murray, L. T., Maasakkers, J. D., and Aben, I.: Evaluating urban methane emissions from space using TROPOMI methane and carbon monoxide observations, Remote Sensing of Environment, 268, https://doi.org/10.1016/j.rse.2021.112756, 2022.

Randerson, J., van der Werf, G., Giglio, L., Collatz, G., and Kasibhatla, P.: Global Fire Emissions Database, Version 4.1 (GFEDv4), https://doi.org/10.3334/ORNLDAAC/1293, 2017.

Ravikumar, A. P., Li, H., Yang, S. L., and Smith, M. L.: Developing Measurement-Informed Methane Emissions Inventory Estimates at Midstream Compressor Stations, ACS ES&T Air, 2, 358–367, https://doi.org/10.1021/acsestair.4c00237, 2025.

Rienecker, M., Suarez, M., Todling, R., Bacmeister, J., Takacs, L., Liu, H.-C., Gu, W., Sienkiewicz, M., Koster, R., Gelaro, R., Stajner, I., and Nielsen, J.: The GEOS-5 Data Assimilation System – Documentation of Versions 5.0.1, 5.1.0, and 5.2.0, Tech. Rep. Technical Report Series on Global Modeling and Data Assimilation, Volume 27 (NASA/TM–2008–104606, Vol. 27), National Aeronautics and Space Administration, Goddard Space Flight Center, Greenbelt, Maryland, https://gmao.gsfc.nasa.gov/pubs/docs/Rienecker369.pdf, 2008.

https://doi.org/10.5194/egusphere-2026-3153
Preprint. Discussion started: 14 August 2026

Rodgers, C. D.: Inverse Methods for Atmospheric Sounding, chap. 5, pp. 92–93, World Scientific, https://doi.org/10.1142/3171, 2000.

Sargent, M. R., Floerchinger, C., McKain, K., Budney, J., Gottlieb, E. W., Hutyra, L. R., Rudek, J., and Wofsy, S. C.: Majority of US urban natural gas emissions unaccounted for in inventories, Proceedings of the National Academy of Sciences, 118, e2105804 118, https://doi.org/10.1073/pnas.2105804118, 2021.

Scarpelli, T. R., Jacob, D. J., Grossman, S., Lu, X., Qu, Z., Sulprizio, M. P., Zhang, Y., Reuland, F., Gordon, D., and Worden, J. R.: Updated Global Fuel Exploitation Inventory (GFEI) for methane emissions from the oil, gas, and coal sectors: Evaluation with inversions of atmospheric methane observations, Atmospheric Chemistry and Physics, 22, 3235–3249, https://doi.org/10.5194/acp-22-3235-2022, 2022a.

Scarpelli, T. R., Jacob, D. J., Moran, M., Reuland, F., and Gordon, D.: A gridded inventory of Canada's anthropogenic methane emissions, Environmental Research Letters, 17, https://doi.org/10.1088/1748-9326/ac40b1, 2022b.

Schiferl, L. D., Cao, C., Dalton, B., Hallward-Driemeier, A., Toledo-Crow, R., and Commane, R.: Multi-year observations of variable incomplete combustion in the New York megacity, Atmospheric Chemistry and Physics, 24, 10 129–10 142, https://doi.org/10.5194/acp-24-10129-2024, 2024.

Schiferl, L. D., Hallward-Driemeier, A., Zhao, Y., Toledo-Crow, R., and Commane, R.: Missing wintertime methane emissions from New York City related to combustion, Atmospheric Chemistry and Physics, 25, 15 683–15 700, https://doi.org/10.5194/acp-25-15683-2025, 2025.

Schuldt, K. N., Aalto, T., Andrade, M., Andrews, A., Apadula, F., Arduini, J., Arnold, S., Baier, B., Bartyzel, J., Bergamaschi, P., Biermann, T., Biraud, S. C., Blanc, P.-E., Boenisch, H., Brailsford, G., Brand, W. A., Brunner, D., Bui, T. P., Burban, B., Bäni, L., Calzolari, F., Chang, C. S., Chen, H., Chmura, L., Climadat, S., Colomb, A., Condori, L., Conen, F., Conil, S., Couret, C., Cristofanelli, P., Cuevas, E., Curcoll, R., Daube, B., Davis, K. J., Mazière, M. D., Dean-Day, J. M., Coletta, J. D., Delmotte, M., Desai, A., Iorio, T. D., DiGangi, J. P., DiGangi, E., Elsasser, M., Emmenegger, L., Forster, G., Frumau, A., Fuente-Lastra, M., Galkowski, M., Gatti, L. V., Gehrlein, T., Gerbig, C., Gheusi, F., Gloor, E., Goto, D., Hammer, S., Hanisco, T. F., Haszpra, L., Hatakka, J., Heimann, M., Heliasz, M., Heltai, D., Henne, S., Hensen, A., Hermans, C., Hermansen, O., Hoheisel, A., Holst, J., Iraci, L. T., Ivakhov, V., Jaffe, D. A., Jordan, A., Joubert, W., Kang, H.-Y., Karion, A., Kazan, V., Keeling, R. F., Keronen, P., Kers, B., Kim, J., Klausen, J., Kneuer, T., Ko, M.-Y., Kolari, P., Kominkova, K., Kort, E., Kozlova, E., Krummel, P. B., Kubistin, D., Kulawik, S. S., Kumps, N., Labuschagne, C., Lan, X., Langenfelds, R. L., Lanza, A., Laurent, O., Laurila, T., Lauvaux, T., Lavric, J., Lee, C.-H., Lee, J., Lehner, I., Lehtinen, K., Leppert, R., Leskinen, A., Leuenberger, M., Levin, I., Levula, J., Lindauer, M., Lindroth, A., Loh, Z. M., Lopez, M., Lowry, D., Lunder, C. R., Löfvenius, M. O., Machida, T., Mammarella, I., Manca, G., Manning, A., Marek, M. V., Marklund, P., Marrero, J. E., Martin, D., Martin, M. Y., Martins, G. A., Matsueda, H., McKain, K., Meinhardt, F., Menoud, M., Metzger, J.-M., Miles, N. L., Miller, C. E., Miller, J. B., Monteiro, V., Montzka, S., Moore, F., Moossen, H., Moreno, C., Morgan, E., Morgui, J.-A., Morimoto, S., Munro, D., Mutuku, M., Myhre, C. L., Mölder, M., Müller-Williams, J., Necki, J., Nichol, S., Nisbet, E., Niwa, Y., Njiru, D. M., Noe, S. M., O'Doherty, S., Obersteiner, F., Parworth, C. L., Peltola, O., Peters, W., Philippon, C., Piacentino, S., Pichon, J. M., Pickers, P., Pitt, J., Pittman, J., Plass-Dülmer, C., Platt, S. M., Popa, M. E., Prinzivalli, S., Ramonet, M., Richardson, S. J., Rigouleau, L.-J., Rivas, P. P., Rothe, M., Roulet, Y.-A., Ryoo, J.-M., Röckmann, T., Santoni, G., Sasakawa, M., Schaefer, H., Scheeren, B., Schmidt, M., Schuck, T., Schumacher, M., Seifert, T., Sha, M. K., Shepson, P., Shin, D., Sloop, C. D., Smale, D., Smith, P. D., Spain, G., Clair, J. M. S., Steger, D., Steinbacher, M., Stephens, B., Sweeney, C., Sørensen, L. L., Taipale, R., Takatsuji, S., Thoning, K., Timas, H., Torn, M., Trisolino, P., Turnbull, J., Vermeulen, A., Viner, B., Vitkova, G., Watson, A., Weiss, R., Weyrauch, D., Wofsy, S. C., Worsey, J., Worthy, D., Xueref-Remy, I., Yates, E. L., Young, D., Yver-Kwok, C., Zaehle, S.,

https://doi.org/10.5194/egusphere-2026-3153
Preprint. Discussion started: 14 August 2026

Zahn, A., Zazzeri, G., Zellweger, C., Zimnoch, M., de Souza, R. A., de Vries, M., di Sarra, A. G., van den Bulk, P., and van der Veen, C.: Multi-laboratory compilation of atmospheric methane data for the period 1981–2024, https://doi.org/10.25925/20241001, 2024.

Shen, L., Zavala-Araiza, D., Gautam, R., Omara, M., Scarpelli, T., Sheng, J., Sulprizio, M. P., Zhuang, J., Zhang, Y., Qu, Z., Lu, X., Hamburg, S. P., and Jacob, D. J.: Unravelling a large methane emission discrepancy in Mexico using satellite observations, Remote Sensing of Environment, 260, https://doi.org/10.1016/j.rse.2021.112461, 2021.

Shen, L., Gautam, R., Omara, M., Zavala-Araiza, D., Maasakkers, J. D., Scarpelli, T. R., Lorente, A., Lyon, D., Sheng, J., Varon, D. J., Nesser, H., Qu, Z., Lu, X., Sulprizio, M. P., Hamburg, S. P., and Jacob, D. J.: Satellite quantification of oil and natural gas methane emissions in the US and Canada including contributions from individual basins, Atmospheric Chemistry and Physics, 22, 11 203–11 215, https://doi.org/10.5194/acp-22-11203-2022, 2022.

Sheng, J. X., Jacob, D. J., Turner, A. J., Maasakkers, J. D., Sulprizio, M. P., Bloom, A. A., Andrews, A. E., and Wunch, D.: High-resolution inversion of methane emissions in the Southeast US using SEAC4RS aircraft observations of atmospheric methane: Anthropogenic and wetland sources, Atmospheric Chemistry and Physics, 18, 6483–6491, https://doi.org/10.5194/acp-18-6483-2018, 2018.

Shindell, D., Kuylenstierna, J. C. I., Vignati, E., van Dingenen, R., Amann, M., Klimont, Z., Anenberg, S. C., Muller, N., Janssens-Maenhout, G., Raes, F., Schwartz, J., Faluvegi, G., Pozzoli, L., Kupiainen, K., Höglund-Isaksson, L., Emberson, L., Streets, D., Ramanathan, V., Hicks, K., Oanh, N. T. K., Milly, G., Williams, M., Demkine, V., and Fowler, D.: Simultaneously Mitigating Near-Term Climate Change and Improving Human Health and Food Security, Science, 335, 183–189, https://doi.org/10.1126/science.1210026, 2012.

Souri, A. H., Nowlan, C. R., González Abad, G., Zhu, L., Blake, D. R., Fried, A., Weinheimer, A. J., Wisthaler, A., Woo, J.-H., Zhang, Q., Chan Miller, C. E., Liu, X., and Chance, K.: An inversion of NO_x and non-methane volatile organic compound (NMVOC) emissions using satellite observations during the KORUS-AQ campaign and implications for surface ozone over East Asia, Atmospheric Chemistry and Physics, 20, 9837–9854, https://doi.org/10.5194/acp-20-9837-2020, 2020.

Staniaszek, Z., Griffiths, P. T., Folberth, G. A., O'Connor, F. M., Abraham, N. L., and Archibald, A. T.: The role of future anthropogenic methane emissions in air quality and climate, npj Climate and Atmospheric Science, 5, 21, https://doi.org/10.1038/s41612-022-00247-5, 2022.

Tarantola, A.: Inverse problem theory : methods for data fitting and model parameter estimation, Elsevier, 1987.

The International GEOS-Chem User Community: GEOS-Chem version 12.2.0, https://doi.org/10.5281/zenodo.2572887, 2019.

The International GEOS-Chem User Community: GEOS-Chem version 14.4.1, https://doi.org/10.5281/zenodo.12584192, 2024.

United Nations Environment Programme: Emissions Gap Report 2024, https://doi.org/10.59117/20.500.11822/46404, 2024.

U.S. Census Bureau: 2018 TIGER/Line Shapefiles: Urban Areas, https://www2.census.gov/geo/tiger/TIGER2018/UAC/, accessed 2025-11-13., 2018.

U.S. Fish and Wildlife Service: National Wetlands Inventory digital data, https://www.fws.gov/program/national-wetlands-inventory, accessed 04 May 2021, 2020.

USGCRP: Second State of the Carbon Cycle Report (SOCCR2): A Sustained Assessment Report, U.S. Global Change Research Program, Washington, DC, USA, https://doi.org/10.7930/SOCCR2.2018, 2018.

van der Werf, G. R., Randerson, J. T., Giglio, L., van Leeuwen, T. T., Chen, Y., Rogers, B. M., Mu, M., van Marle, M. J. E., Morton, D. C., Collatz, G. J., Yokelson, R. J., and Kasibhatla, P. S.: Global fire emissions estimates during 1997–2016, Earth System Science Data, 9, 697–720, https://doi.org/10.5194/essd-9-697-2017, 2017.

Varon, D. J., Jacob, D. J., Sulprizio, M., Estrada, L. A., Downs, W. B., Shen, L., Hancock, S. E., Nesser, H., Qu, Z., Penn, E., Chen, Z., Lu, X., Lorente, A., Tewari, A., and Randles, C. A.: Integrated Methane Inversion (IMI 1.0): a user-friendly, cloud-based facility for inferring high-resolution methane emissions from TROPOMI satellite observations, Geoscientific Model Development, 15, 5787–5805, https://doi.org/10.5194/gmd-15-5787-2022, 2022.

Wei, Y., Shrestha, R., Pal, S., Gerken, T., Feng, S., McNelis, J., Singh, D., Thornton, M. M., Boyer, A. G., Shook, M. A., Chen, G., Baier, B. C., Barkley, Z. R., Barrick, J. D., Bennett, J. R., Browell, E. V., Campbell, J. F., Campbell, L. J., Choi, Y., Collins, J., Dobler, J., Eckl, M., Fiehn, A., Fried, A., Digangi, J. P., Barton-Grimley, R., Halliday, H., Klausner, T., Kooi, S., Kostinek, J., Lauvaux, T., Lin, B., McGill, M. J., Meadows, B., Miles, N. L., Nehrir, A. R., Nowak, J. B., Obland, M., O'Dell, C., Fao, R. M. P., Richardson, S. J., Richter, D., Roiger, A., Sweeney, C., Walega, J., Weibring, P., Williams, C. A., Yang, M. M., Zhou, Y., and Davis, K. J.: Atmospheric Carbon and Transport – America (ACT-America) Data Sets: Description, Management, and Delivery, Earth and Space Science, 8, e2020EA001 634, https://doi.org/10.1029/2020ea001634, 2021.

Worden, J. R., Cusworth, D. H., Qu, Z., Yin, Y., Zhang, Y., Bloom, A. A., Ma, S., Byrne, B. K., Scarpelli, T., Maasakkers, J. D., Crisp, D., Duren, R., and Jacob, D. J.: The 2019 methane budget and uncertainties at 1º resolution and each country through Bayesian integration of GOSAT total column methane data and a priori inventory estimates, Atmospheric Chemistry and Physics, 22, 6811–6841, https://doi.org/10.5194/acp-22-6811-2022, 2022.

Xu, J., Morris, P. J., Liu, J., and Holden, J.: PEATMAP: Refining estimates of global peatland distribution based on a meta-analysis, Catena, 160, 134–140, https://doi.org/10.1016/j.catena.2017.09.010, 2018.

Yuan, B., Kaser, L., Karl, T., Graus, M., Peischl, J., Campos, T. L., Shertz, S., Apel, E. C., Hornbrook, R. S., Hills, A., Gilman, J. B., Lerner, B. M., Warneke, C., Flocke, F. M., Ryerson, T. B., Guenther, A. B., and de Gouw, J. A.: Airborne flux measurements of methane and volatile organic compounds over the Haynesville and Marcellus shale gas production regions, Journal of Geophysical Research: Atmospheres, 120, 6271–6289, https://doi.org/https://doi.org/10.1002/2015JD023242, 2015.